Large Diameter Drilling Performance and Imaging Fluid Optimization

By

©Oluwatimilehin Mary Akindele

A thesis submitted to the School of Graduate Studies In partial fulfillment of the requirements

for the degree of

Master of Engineering

Faculty of Engineering and Applied Sciences

Memorial University of Newfoundland

St John's, Newfoundland and Labrador

October 2024

Abstract

Large diameter drilling is a critical practice across industries such as mining, energy, marine, and construction. Ensuring precision, efficiency, and accurate estimation of time and costs is paramount for the success of capital-intensive projects involving substantial investments. This thesis presents a broad exploration into the optimization of large diameter drilling operations, focusing on unraveling intricate facets that significantly impact rock excavation performance. The multifaceted approach encompasses borehole imaging, imaging fluid properties and optimization, cuttings cleaning efficiency, and 3D scanning for volume estimation. Borehole imaging tools play a crucial role in creating signals reflected from the ground, providing insights into borehole structural features. The study recognizes the importance of imaging fluids in mitigating the impact of borehole groundwater on imaging data quality. Innovative use of 3D scanning for volume estimation offers precise measurements of rock chip volume, facilitating specific energy calculations and optimizing drilling operations. Moreover, findings on cuttings cleaning efficiency underscore its critical role in drilling performance, with direct implications for overall efficiency and cost-effectiveness. Results indicate observed relationships between drilling performance and the adopted cleaning efficiency. Under the same applied weight on bit (WOB) and rotary speed, the drilling performance (rate of penetration, drilling torque, and cuttings size distribution) was higher for the wet drilling setup unlike that of dry drilling. This suggests that wet drilling methods enhance cuttings cleaning efficiency. Exploration of imaging fluid rheological properties enhances understanding, offering practical insights for fluid optimization under diverse conditions. It was observed that the temperature of the fluid mixture before the addition of barite plays a significant role in the stability of the fluid. Notably, the development of a water-based imaging fluid addresses environmental and cost concerns, demonstrating comparable performance to oil-based

counterparts. These findings suggest the potential viability of the water-based fluid for borehole Ground Penetrating Radar (GPR) applications, offering environmentally friendly and cost-effective solutions. Overall, this research contributes to enhancing the planning, design, and execution of large diameter drilling projects, with implications for precision, efficiency, and cost-effectiveness in varied geological formations. The findings provide a robust foundation for future research and practical applications in the field of large diameter drilling.

Acknowledgments

I want to express my deepest gratitude to God and to the following individuals whose unwavering support and guidance have been instrumental in successfully completing my master's program.

First and foremost, I am immensely thankful to my supervisor, Dr. Stephen Butt, and co-supervisor, Dr Yusuf Babatunde, for their invaluable mentorship, encouragement, and scholarly insights throughout this academic journey. Their expertise and commitment to academic excellence have been a guiding light, shaping my research's content and structure.

Heartfelt thanks to the laboratory manager, Dr. Abdelsalam Abugharara and the entire Drilling Technology Laboratory (DTL) group members who provided unwavering support, shared insights, and made the academic journey memorable. Your camaraderie made the challenges more manageable and the successes more joyous.

I owe a special debt of gratitude to my spouse, David Akindele, whose unwavering love, encouragement, and understanding have been my pillars of strength. Your support made the late nights and intense study sessions more manageable, and your belief in my abilities fueled my determination. I am also indebted to my family for their unconditional love and support, which sustained me during challenging times. Their unwavering belief in my abilities has been a constant source of motivation.

Last but not least, I want to express my gratitude to Memorial University of Newfoundland, Novamera Inc, and MITACs for their financial and technical support, which played a crucial role in enabling me to focus on my studies and research.

Co-authorship Statement

I, Oluwatimilehin Akindele, hold the primary author status for all Chapters in this thesis except Chapter 5. Chapter 5 manuscript was prepared by me, Oluwatimilehin Mary Akindele, and Leila Abbasian for publication. However, each manuscript is co-authored by my supervisor and external research collaborators. The contributions of each of the co-authors are listed below:

- Chapter 3 is authored by Oluwatimilehin Mary Akindele, Judith Onyedikachi George, Abdelsalam Abugharara, and Stephen Butt. "**Impact of Cleaning Efficiency on Disc Cutter Drilling Performance**" Proceedings of the ASME 2023 42nd International Conference on Ocean, Offshore and Arctic Engineering, OMAE 2023. https://doi.org/10.1115/OMAE2023-108187

Statement: The research was conducted by Oluwatimilehin Mary Akindele as the first author. She prepared the manuscript based on the research outcome. Judith Onyedikachi George provided the experimental data. Other authors supervised the student, reviewed the manuscript, and provided feedback.

- Chapter 4 is authored by Oluwatimilehin Mary Akindele, Abdelsalam Abugharara, and Stephen Butt. "**Volume Estimation for Unrelieved Mode of Cutting**" A technical note prepared for submission.

Statement: The research was conducted by Oluwatimilehin Mary Akindele as the first author. She prepared the manuscript. Dr. Abdelsalam Abugharara assisted with the experiment implementation while Dr. Stephen Butt supervised the student, reviewed the manuscript, and provided feedback.

- Chapter 5 is authored by Leila Abbasian, Oluwatimilehin Mary Akindele, Abdelsalam Abugharara, and Stephen Butt. "**Effect of Preparation Method and Weighting Agent**

Particle Size on Imaging Fluid Quality and Rheological Properties" Manuscript has been accepted to be published at ARMA Golden 2024.

Statement: The research was conducted together by Oluwatimilehin Mary Akindele and Leila Abbasian. I and Leila prepared the manuscript for publication. Other authors supervised the students, reviewed the manuscript, and provided feedback.

- Chapter 6 is authored by Oluwatimilehin Mary Akindele, Abdelsalam Abugharara, and Stephen Butt. "**Water Based Alternative for Imaging Fluid**" Manuscript prepared for publication.

Statement: The research was conducted by Oluwatimilehin Mary Akindele as the first author. She prepared the manuscript. Leila Abbasian reviewed the experimental plan, Dr. Abdelsalam Abugharara assisted with the experiment implementation while Dr. Stephen Butt supervised the student, reviewed the manuscript, and provided feedback.

Table of Contents

List of Figures

List of Tables

Nomenclature

ρ_b	Bulk Density (kg/m^3)
ν_p	Compressive Wave Velocity (m/s)
E'	Dynamic Modulus (GPa)
EM	Electromagnetic
GPR	Ground Penetrating Radar
HT	High Temperature
σ_t	Indirect Tensile Strength (MPa)
LT	Low Temperature
E	Modulus of Elasticity (GPa)
PV	Plastic Viscosity
σ_{PLI}	Point Load Strength Index
ν	Poisson Ratio
ROP	Rate of Penetration (cm/min)
RDP	Relative Dielectric Permittivity
ν_s	Shear Wave Velocity (m/s)
SG	Specific Gravity
3D	Three Dimensional
T	Torque (Nm)
TBM	Tunnel Boring Machine
UCS	Unconfined Compressive Strength (MPa)
WOB	Weight on Bit (KN)
YP	Yield Point

1. Introduction

1.1 Background of the Thesis

This thesis focuses on three areas relevant for optimizing large diameter drilling and emerging mining technologies centered on developing sustainable mining methods where the ore is mined as drill cuttings using directional large diameter drilling guided by high resolution subsurface imaging. Large diameter drilling finds application in various industries such as mining, energy, marine and construction with disc cutters as the predominant tool for drilling of both soft and hard rocks. Given the high capital investment involved, precise planning, design, and accurate prediction of drilling projects are essential for estimating time and costs accurately. Regardless of the hole drilled or the rock excavated, rock excavation performance optimization remains a concern. Drilling performance is significantly impacted by the geological conditions, including rock properties and discontinuities, as well as drilling operational conditions [1]. This encompasses insights gained through borehole imaging to the design of cutter geometry, cutting pattern, and the cuttings evacuation method.

The borehole imaging technology tool helps to create signals reflected from the ground, which, when interpreted, can give an indication of the borehole structural features and contour determination, to mention a few. The Imaging tool's directionality function and the Survey tool's positioning feature work together to facilitate the navigation of the pilot hole through the foot wall and hanging wall's center. To accurately capture these signals with good quality GPR data, the impact of the borehole ground water on GPR imaging needs to be avoided. Borehole water needs to be replaced by an imaging fluid at the bottom hole with the imaging tool completely immersed in the fluid during imaging. The imaging fluid should have similar dielectric properties as the host

rock; low conductivity (low EM wave attenuation), appropriate dielectric permittivity (to avoid signal ringing between the fluid-wellbore boundary), higher density than water (to stay at the bottom hole) and stability (avoid discomposing during the imaging). To better understand the stability of imaging fluid in water, it is important to study the rheological properties of the fluid. This is because the capacity of any fluid to perform its specific functions greatly depends on its rheological characterization [2].

The cutter head drives the disc cutters to constantly cut the rock mass during the large diameter drilling operation. A better understanding of rock cutter interaction and fundamental rock breakage phenomena will aid in its successful application and efficient use. This has drawn a lot of attention from researchers as it should be noted that the primary cause of rock failure is the interaction between the cutter and the rock, and that the geometric shape of the contact body is a key determinant of the contact behavior. Prediction of the rock excavation performance of large diameter drilling using disc cutter for any geological formation is one of the main concerns in determining the economics of the drilling operation as proper understanding of rock fragmentation mechanism is the foundation of efficient cutters selection, design, arrangement, and operation optimization.

1.2 Research Objective

The overarching objective of this research is to enhance the understanding of large diameter drilling using disc cutters, focusing on optimizing rock excavation performance. This involves in-depth investigations into borehole imaging, imaging fluid, imaging fluid stability, interaction between disc cutters and rock formations, excavated rock volume estimation for an unrelieved cutting mode, and the efficiency of a drilling operation. The research aims to contribute valuable

insights that can inform the planning, design, and execution of large diameter drilling projects across diverse geological formations.

1.3 Thesis Outline

This thesis consists of seven (7) chapters that sequentially address different facets of large diameter drilling. The description of each chapter is as follows:

Chapter 1: Introduction which describes the overview and a summary of this thesis. This chapter includes a background of the thesis content, research objectives, and a preview of each chapter's contents.

Chapter 2: Literature review that includes a broad concept of large diameter drilling, focusing on the critical role of disc cutters and their impact on rock fragmentation. The review explores various aspects, including rock breaking mechanisms, failure modes, factors affecting drilling efficiency, disc spacing optimization, cleaning efficiency, and descriptors for measuring drilling performance, along with an introduction to borehole Ground Penetrating Radar technology, its principles, material properties, and the importance of an ideal imaging fluid for accurate subsurface mapping during drilling.

Chapter 3: represents the publication of a technical paper at OMAE 2023 and additional research. This chapter explains the influence of cutting cleaning efficiency on the performance of large diameter drilling operations, specifically employing disc cutters. Through two sets of experiments using the same drilling parameters but different cuttings evacuation methods (dry and wet), the study reveals the cleaning method that provides an improved cleaning efficiency, through higher rates of penetration, drilling torque, and cuttings size distribution highlighting the importance of effective cuttings removal in optimizing drilling operations.

Chapter 4: is a study that provides a detailed approach to a new method of determining rock volume excavated in a drilling operation, using a 3D scanner, for an unrelieved cutting mode. The findings demonstrate the application of the 3D scanner in capturing and analyzing cutter groove profiles, enabling precise measurement of rock chip volume crucial for calculating specific energy in large diameter drilling operations.

Chapter 5: is a technical paper scheduled to be published at ARMA Golden 2024 conference investigating the impact of agitation, temperature, and weighting agent particle size on the quality of oil-based imaging fluid used in borehole imaging technology. The study analyzes the stability, settling and rheological properties of the prepared imaging fluid for quality.

Chapter 6: is research exploring the development of a water-based alternative imaging fluid for Ground Penetrating Radar (GPR) applications, addressing challenges posed by existing oil-based imaging fluids. The potential of the proposed fluid as a sustainable solution for borehole imaging was studied through conductivity measurement and performing GPR simulations.

Chapter 7: provides a summary and conclusion for the study presented related to large diameter drilling performance and imaging fluid optimization.

2. Literature Review

Large diameter drilling has found extensive applications in mining engineering, water conservancy, hydropower tunnels, highway tunnels, and various projects. The disc cutter, positioned at the leading end of the TBM, plays a crucial role as they are in direct interaction with the rocks [3]. Its effectiveness determines the machine's ability to efficiently break rock, exerting direct pressure on the surrounding rock to induce dynamic damage to the rock mass [4].

2.1 Rock Fragmentation Mode

Rock fragmentation is a critical process in drilling operations, influencing not only the efficiency of the drilling process but also downstream activities such as excavation and mineral extraction. Rock cutting involves fracturing and fragmentation of a rock through methods and utilizing different machines [5]. Understanding rock fragmentation is essential for optimizing drilling operations. According to Yagiz et al. [6], the effectiveness of a tunnel boring machine is contingent on the rock breaking mechanism initiated by disc cutters. In general, the traditional rock breaking mechanism of the cutter can be explained as follows: as the cutter's penetration depth increases, the rock at cutter tip first forms a high stress crushing zone, and then the cracks from the crushing zone start to extend below and sideways, respectively, to form vertical and lateral cracks as shown in Figure 2-1 below [7]. Zhang et al.in 2022 [3] concluded from his research that both tensile and shear cracks manifest simultaneously in the failure zone beneath the disc cutter edge, with a prevalence of shear cracks over tensile cracks. The rock breaking process by the disc cutter exhibits characteristics of compaction, shearing, and tensile failure modes.

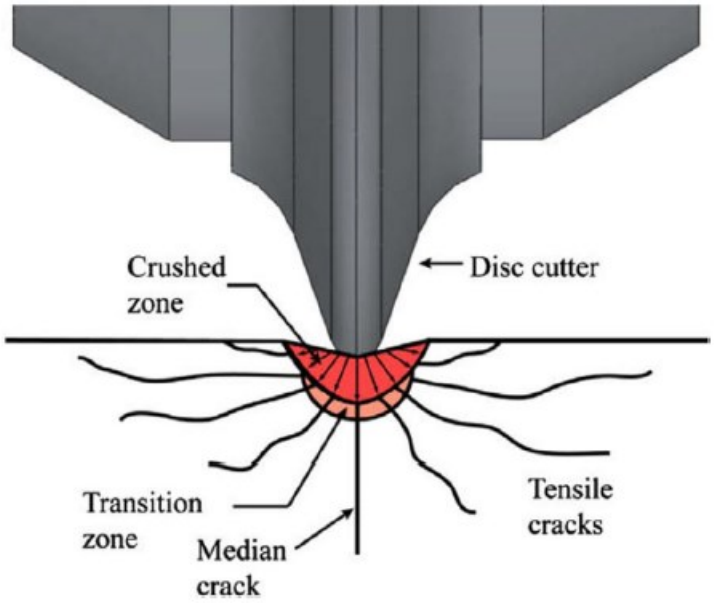

Figure 2-1: Disc cutter rock failure mechanism during cutting [8]

Xia et al. [9], Xu et al. [10], and Zhang et al. [11] found that rock fragments are created when these cracks spread to the free surface or connect to cracks created by a neighbouring cutter. By executing the aforementioned rock breaking procedure, TBMs are able to achieve high-efficiency tunnelling in rock environments with varying strengths. However, when TBMs encounter large burial depths, highly abrasive rock, and extremely hard rock, the cutter's penetration depth and excavation efficiency significantly decrease. This is accompanied by issues like abnormal damage to the disc cutter and cutter head, which has a negative impact on the drilling project [7].

There are several methods of performance prediction under different cutting condition and the best approach may be the use of more than one of these methods. These methods may be generally classified as the laboratory test which involves the full-scale linear cutting test and the small-scale cutting test (core cutting), empirical approach, theoretical analysis, numerical simulation, and field study [12].

Studies on the rock fragmentation process can be divided into the following categories.

i Study of the indentation process in laboratory tests (standard indicator of material hardness)

ii Rock fracture test

iii Investigation of the rock cutting process by using full scale tests in the laboratory under controlled conditions

iv Analysis of stress distribution beneath the disc cutter

v Evaluation of the machine performance and geological parameters in the field

Study of the indentation process has greatly advanced our understanding of the mechanism of crushed zone formation and the growth of cracks, but it has fallen short of providing the broader picture of chip formation and the interaction of all cutting parameters in disc cutting operation [13]. Conducting experiments in a laboratory setting provides fundamental data for the selection of the most appropriate cutting tool and the design of a disc cutting head tailored to a particular rock mass [14].

Extensive research has been carried out to offer valuable insights for the design and enhancement of TBMs' capacity to cut rock. These studies have considered several aspects such as the configuration and structure of the cutter, drilling parameters, and the characteristics of the rock. For example, studies showed that as the space between two adjacent cutters increased, so is their cutting force and the volume of rock fragments produced initially increased and subsequently reduced. The lowest ratio of the cutter's work to the volume of rock pieces (i.e., the amount of energy needed for the cutter to cut a unit volume of rock) indicates the presence of an optimized cutter spacing [15–16]. An innovative TBM disc cutter with spiral grooves was investigated for rock-cutting and wear [17] by Zhang et al. When employing TBM disc cutters to cut certain British rocks, Snowdon et al. [18] examined the effects of excavation features by penetration depth and spacing. Gertsch et al. [19] analyzed the fragmentation mechanism to predict the performance of a TBM from the disc cutting test of Colorado red granite. Zhang K. et al. [20] proposed a two- step simulation modeling method of rock breaking of TBM disc cutters assisted with lasers for better

understanding of rock fragmentation. Frengchao Wang et al. [21] also did a study to investigate disc cutter rock breaking performance when assisted by high-pressure water jet.

Balci et al.'s study [22] looked into estimating the ideal specific energy based on the characteristics of the rock in order to evaluate roadheader performance using linear cutting tests. Using a number of descriptor techniques for chip size distribution, Wang et al. [23] examined the efficiency of rock-cutting in both relieved and unrelieved cutting circumstances. Indentation experiments were used by Huang et al. [24] to examine the features of granite excavation beneath conical picks.

The mechanism of failure of the rock under the disc cutter explains the pattern of cut obtained on the rock surface. There are two main mechanisms of rock failure: crushing (under each disc due to the applied compressive load) and tensile failure (chipping resulting from the connection of the cracks created and propagated between adjacent grooves).

Crushing produces highly fractured, little rock fragments in the form of chips that resemble powder, whereas chipping starts and propagates fractures to produce large rock fragments, i.e., chunk-like rock chips [25]. Fracture mechanics has attributed many explanations for the chipping and crushing modes, e.g., tensile [26], shear [27], or tensile-shear hybrid fractures [28]. Studies have revealed that rock breakage occurs because of the complex interaction of multiple micro-cracks produced under tensile stress. Figure 2-2 below shows the failure mechanism in rock shearing when the cutter contacts with the rock. As soon as the cutter makes initial contact with the rock, a compact damage zone beneath the cutter's front face is created, as seen in Fig. 2-2a. The tight damage zone then expands during the crushing process as microcracks turn into macrocracks. In Fig. 2-2b, some of the macro-cracks at this stage first penetrate the free surface of the virgin rock to produce numerous extensively fragmented small rock particles that resemble rock chips. After crushing, the rock failure progresses to chipping, in which the macrocracks in

the compact damage zone keep expanding and fusing together. When a conglomerate of macro-cracks reaches the free surface of the rock, large rock fragments, specifically chunk-like chips, are eventually produced shown in Fig 2-2c [25].

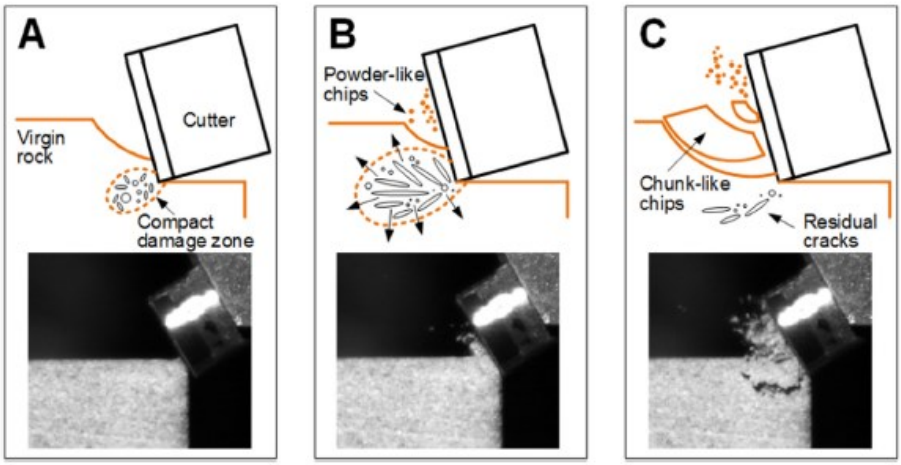

Figure 2-2: Rock failure mechanisms in shearing: (A) Micro-crack nucleation, (B). Crushing phenomenon, and (C) Chipping phenomenon [25]

The combined impact of these two mechanisms results in the removal of the complete exposed half-space of the rock. This mode of cutting is named relieved cutting as a uniform cross-sectional area of rock is removed per unit time as seen in Figure 2-3a below. To achieve relieved cutting, the rock properties (shear strength, compressive strength, rock quality designation), disc cutter geometry (including the angle at the tip) as well as the spacing between subsequent cuts play a significant role (Fig. 2-3b).

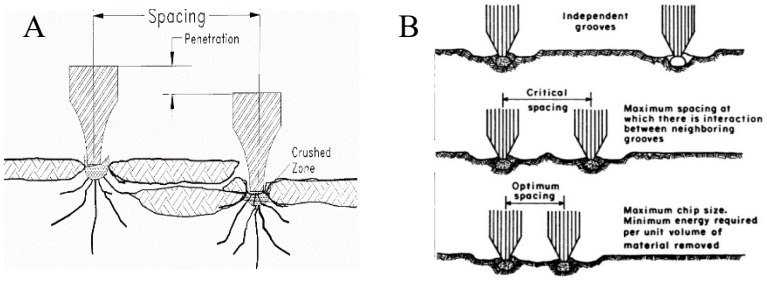

Figure 2-3: A) Relieved disc cutting mode - interactive grooves [29] B) Optimum and critical cutter spacing [30]

When the cutting of the rock is attributable to crushing under the discs as well as side forces due to cutting at tight radii, this pattern of cutting is called unrelieved cutting. It is often observed on high-strength intact rocks especially when the spacing between the discs is too high for the micro cracks to coalesce and propagate to the free surface [29]. The maximum distance between two adjacent parallel grooves cut at which there is interaction between grooves is referred to as critical spacing. The grooves become independent at spacings greater than the critical spacing, and with a closer spacing, there is chipping between neighboring grooves. Compared to independent grooves, the chips created by breakout between interacting grooves are significantly larger. There is an ideal spacing for any set of drilling parameters where most cuttings are produced with the least amount of specific energy. Reduced cutting efficiency as measured by cutting weight and specific energy will occur from any decrease or increase in groove spacing from the optimal spacing [30].

2.2 Factors Affecting Drilling Efficiency

- Rock properties: This consists of the hardness, abrasiveness, and compressive strength of the rock. This factor can significantly influence tool wear and the overall drilling performance as harder, abrasive, and high compressive strength rocks require more force and energy to drill. While drilling parameters can be controlled, changes to the rock properties cannot be controlled and so understanding these rock properties is crucial for selecting appropriate drilling equipment, optimizing drilling parameters, and ensuring the overall efficiency and success of drilling operations in diverse geological conditions [31,32].
- Cutter geometry/ design: Key considerations under this involve cutter shape and configuration, cutter size and arrangement, cutter material and coatings, cutter penetration mechanism, and its orientation and angles. Optimizing rock cutter geometry and design is crucial for achieving

higher drilling efficiency, reducing downtime, and extending the lifespan of drilling tools [3,33-39].

- Disc spacing: refers to the arrangement or distance between disc cutters on a drilling tool. It is a crucial parameter in the design and operation of drilling tools with notable impact on drilling efficiency. Its optimization enhances overall performance (effective rock breaking and efficient drilling operations) in various drilling applications. Disc spacing influences drilling efficiency in several ways such as the penetration pattern, contact area and force distribution, prevention of tool overlapping, cuttings removal efficiency, vibration control, and drilling accuracy. [4,5,8,39-40]. Figure 2-4 shows the rock breaking mechanism using disc cutter with large, small, and optimum cutter spacing.

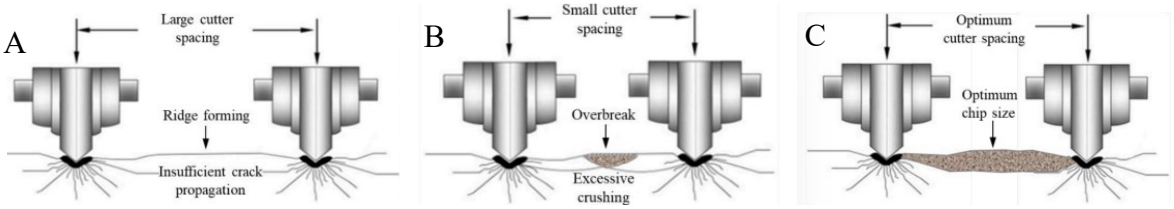

Figure 2-4: Rock breaking by tbm adjacent cutters (A) Ridge formation with a large cutter spacing (B) Excessive crushing with a small cutter spacing (C) Chip formation with an optimal cutter spacing [40]

- Cleaning efficiency: The cleaning mode employed in a drilling operation has a substantial impact on overall drilling efficiency. The cleaning mode refers to the method and system used to remove cuttings and debris from the borehole during drilling. A study on this is explained in Chapter 3 where two different cleaning mode laboratory experiment was done to investigate its impact on drilling efficiency.

2.3 Descriptors to Measure Drilling Performance

Measuring drilling performance involves assessing various parameters and descriptors that collectively provide insights into the efficiency, effectiveness, and success of drilling operations. Here are key descriptors commonly used to measure drilling performance [41-44]:

- Penetration depth: this refers to the depth at which the drill bit advances into the rock.
- Rate of Penetration (ROP): This quantifies the depth drilled per unit of time, providing a numerical measure of drilling speed.
- Cuttings size analysis: This refers to the size distribution of the cuttings produced during drilling operations, larger cuttings size gives an indication of a more efficient drilling operation and performance.
- Specific energy: This is computed by taking into consideration the amount of cutting volume produced in a drilling operation. Depending on the drilling parameters and mechanism of failure of the rock, the cutting mode can either be relieved or unrelieved. With unrelieved cutting mode, it is quite challenging to estimate the volume of rock surface removed per unit time which is needed for specific energy computation. Further study on this is captured in Chapter 4.

2.4 Ground Penetrating Radar

Ground penetrating radar (GPR) is utilized across various fields due to its versatility and has been widely employed and successful in borehole inspection and imaging for mineral resource exploration. GPR uses geophysical technique to acquire detailed information about the subsurface with exceptionally high resolution. It uses high frequency electromagnetic waves to map out the downhole subsurface geology [45]. GPR has been used for surveying many different types of geological strata, ranging from exploration of the Artic and Antarctic icecaps and the permafrost regions of North America to mapping of granite, limestone, marble, and other hard rocks as well as geophysical strata [46]. The field of GPR applications has experienced rapid growth over the past 15 to 20 years, witnessing significant advancements in theories, techniques, and technology [47]. In 1994, Peters et.al. [48] described Ground Penetrating Radar as a radar system designed

specifically to locate and characterize structures beneath the ground's surface. Its specifications, including frequency and bandwidth, are tailored to detect the intended targets, whether they are natural formations or human-made objects, even in challenging environments characterized by lossy and potentially uneven media. Factors such as propagation losses, antenna dimensions, and the size of the target being sought determine the operational frequency band.

Ground-penetrating radar (GPR) is a non-destructive method that involves using a transmitting antenna to emit electromagnetic (EM) energy in the form of radio waves, typically within the frequency range of 10 to 1000 MHz, into the ground to detect targets. GPR operates based on the principle of scattering EM waves, which are reflected back when encountering changes in the characteristics of the target [49]. GPR operates by sending out brief electromagnetic pulses into the ground and capturing the echoes that bounce back. The changes in the signal over time as it travels through various underground materials and encounters reflections are recorded as a sequence of data points at the receiver. These reflections reveal characteristics such as underground layers, specific obstacles like rebar or metal elements, pipelines, and various geological structures [50]. When an EM wave encounters a target, it undergoes partial reflection back to the antenna receiver as it transitions between different mediums. The strength of the reflected signal depends on the difference in dielectric constant between these mediums. Important wave properties are the wave velocity, wave attenuation, amplitude, and the EM wave impedance. A key consideration with GPR is signal attenuation, where higher frequencies offer greater resolution but less depth penetration, while lower frequencies provide deeper information at the expense of resolution [49].

The operational effectiveness of GPR depends on fulfilling the following criteria [46]:

- Effective transmission of electromagnetic radiation into the ground.

- Sufficient penetration of the radiation through the ground, considering the desired depth of target detection.
- Acquisition of a sufficiently strong scattered signal from buried objects or dielectric changes for detection at or above the ground surface.
- Ensuring a suitable bandwidth in the detected signal, considering the desired resolution and noise levels.

In general, the GPR method comprises two approaches: the GPR Surface method and the GPR Borehole method. In the Surface method, the GPR tool remains positioned above ground level while collecting data. Conversely, in the Borehole method, the tool is inserted between existing objects/structures, or the object/structure being detected [51]. Ground penetrating radar systems have a straightforward concept: they aim to measure the amplitude of the field over time following excitation. The amplitude of the reflected signal is dependent upon the difference in dielectric constant between the two mediums. At the core of a GPR system, as depicted in Figure 2-5, lies the timing unit, responsible for managing signal generation and detection. While many GPR systems operate in the time domain, there is a growing trend towards employing frequency domain measurements to replicate time domain responses [52].

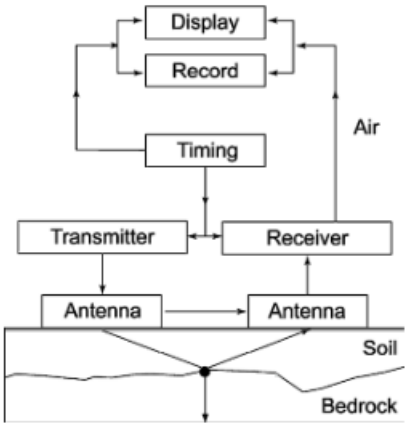

Figure 2-5: Block diagram illustrating main components of a GPR system [52]

2.4.1 GPR Basic Principles

The core principles of ground penetrating radar (GPR) are based on electromagnetic (EM) theory. This overview delineates the essential components necessary for conducting quantitative analyses in GPR. Maxwell's equations provide the mathematical foundation for comprehending the physics of EM fields, while constitutive relationships quantify the characteristics of materials. By combining these elements, the groundwork is laid for quantitatively interpreting GPR signals [47, 52].

Mathematically, EM fields and relationships are given as follows [52]:

$$\overline{\nabla} \times \bar{E} = -\frac{\partial \bar{B}}{\partial t} \qquad (2\text{-}1)$$

$$\overline{\nabla} \times \overline{H} = \bar{J} + \frac{\partial \bar{D}}{\partial t} \qquad (2\text{-}2)$$

$$\overline{\nabla} \ . \ \bar{D} = q \qquad (2\text{-}3)$$

$$\overline{\nabla} \ . \ \bar{B} = 0 \qquad (2\text{-}4)$$

Where:

$\bar{E}$ – Electric field strength vector (V/m)

$\bar{B}$ – Magnetic flux density vector (T)

$\overline{D}$ – Electric displacement vector

$\overline{H}$ – Magnetic field intensity vector (A/m)

q – Electric charge density (C/m^3)

$\bar{J}$ – Electric current density vector (A/m^2)

T – Time (s)

Maxwell's equations mentioned above summarized the findings of various researchers in a concise form and described the connection between the electric and magnetic fields, which mutually induce each other and are perpetually perpendicular to one another (refer to Figure 2-6).

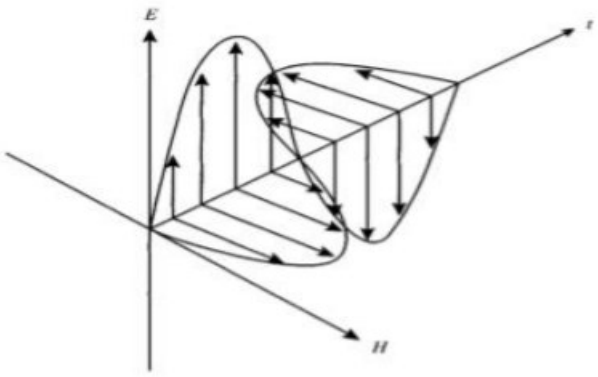

Figure 2-6: EM waves propagation in free space [46]

Constitutive relationships help to quantify the characteristics of materials and its response to EM fields. It provides information about the average behavior of electrons, atoms, and molecules in the EM field, which is of importance to GPR [52,53].

$$\bar{J} = \bar{\sigma}\bar{E} \qquad (2\text{-}5)$$

$$\bar{D} = \bar{\varepsilon}\bar{E} \qquad (2\text{-}6)$$

$$\bar{B} = \bar{\mu}\bar{H} \qquad (2\text{-}7)$$

Where $\bar{\sigma}, \bar{\varepsilon}, \bar{\mu}$ are tensors and constitutive parameters representing electrical conductivity, dielectric permittivity, and magnetic permeability of the medium respectively.

2.4.2 Material Properties

Electromagnetic wave propagation in a medium is dependent on the electric properties of the material as GPR is most useful in low-electrical loss materials, it determines the depth at which the signals would penetrate. In a real-life scenario, low electrical loss conditions are not common [52]. For example, boreholes filled with groundwater can create a situation with very limited GPR

signal penetration because of their electrical properties. These properties are the material electrical conductivity, relative dielectric permittivity (dielectric constant), and magnetic properties.

2.4.2.1 Electrical Conductivity

Electrical conductivity is indicative of the ease with which free charges move, generating electric current when exposed to an electric field. Resistance to the flow of charge results in the dissipation of energy. Increasing electrical conductivity poses a challenge to the penetration of EM waves. Multiples or "ring-down" phenomena in GPR data manifest when EM waves encounter conductive materials or mediums, such as metals, along their path. Upon interaction with EM waves, these metals act as additional antennas, amplifying and transmitting EM waves, consequently leading to the occurrence of "ring-down" in GPR data [47, 52].

2.4.2.2 Relative Dielectric Permittivity

Permittivity characterizes a material's capacity to store and discharge electromagnetic (EM) energy through electric charge, traditionally associated with the storage capability of capacitors. The relative permittivity, often termed the 'dielectric constant' and denoted by the symbol (κ), quantifies this property [54]. The duration for an EM wave to traverse from the transmitter through the subsurface to the receiver hinges on the relative dielectric permittivity of both the transmitting and reflecting mediums. Various materials exhibit varying dielectric permittivity, reflecting their capacity to store electrical charge. The quantity of reflected energy acquired is contingent upon the variance in dielectric permittivity between the two materials as the EM wave progresses from one medium to another [47].

2.4.2.3 Magnetic Permeability

Magnetic permeability denotes the response of intrinsic atomic and molecular magnetic moments to a magnetic field. In simple materials, the distortion of intrinsic magnetic moments facilitates the storage of energy within the material [52]. Under most conditions, magnetic permeability is not considered to play a major role in GPR except when the rocks have high magnetic susceptibility.

2.4.3 EM Compactible Imaging Fluid

Imaging waves respond to variations in the subsurface and to contrasts in electrical and magnetic properties, allowing the identification, visualization, and description of such changes. This imaging data quality is sensitive to the presence of borehole water or the media between the antenna and the wellbore. Hence the need for an imaging borehole fluid that's able to mitigate the impact of ground water on imaging data quality. From research, the ideal borehole fluid (imaging fluid) should have dielectric properties close to that of the host rock. These properties include;

- Low conductivity for low electromagnetic wave attenuation
- Appropriate dielectric permittivity close to the host rock to prevent signal ringing between the fluid-wellbore boundary.
- Density greater than water to allow its settlement at the bottom of the hole.
- High stability such that it does discompose during imaging.

To achieve the above properties, the imaging fluid is made up of a fluid base with low dielectric permittivity and conductivity, a weighting agent to increase its density and an emulsifier to ensure its stability.

2.5 GPR Modeling

Modeling Ground Penetrating Radar (GPR) responses is crucial for enhancing our comprehension of GPR technology and borehole imaging fluid and for testing novel data processing methods. Numerous authors have documented successful modeling endeavors of GPR, with many relying on the finite-difference time-domain (FDTD) method. This modeling is done using a software tool called GprMax (one of many software that can be used for finite-difference modeling of GPR data); It is an open-source software that simulates the transmission of electromagnetic waves employing the Finite Difference Time Domain (FDTD) technique for numerically modeling GPR, and the output from the software is represented using A-Scan and B-Scan signal. A-scan represents the model time history of the electric and magnetic field components and currents at the receiver. It is the amplitude of the reflected waves as a function of time, while a B-scan is composed of multiple traces (A-scan) recorded as the receiver is moved from the borehole into the rock [54, 55]. GPRMax has helped in a deeper understanding of GPR operations and detection mechanisms. In using GPRMax, some input commands are necessary to construct a model. These commands can be seen in Figure 2-7 below.

Command	Function
#domain:	Controls the physical size of the model
#dx_dy:	Defines the discretization steps
#time_window:	Defines the simulated time window for the GPR trace
#medium:	Introduces the electrical properties of different media in the model
#box:	Introduce a rectangle of specific properties into the models space
#cylinder:	Like the box: but introduces a cylinder into the model
#triangle:	Like the box: but introduces a triangular patch.
#tx:	Specifies the details of a transmitter (Tx)
#rx:	Specifies the details of a receiver (Rx)
#scan:	Can be used to automatically generate B-Scans

Figure 2-7: A table showing some GPRMax 2D commands [56]

3. Impact of Cleaning Efficiency on Disc Cutter Drilling Performance

This chapter discusses the impact of cleaning efficiency on disc cutter drilling performance. It is based on a technical paper published on the proceedings of the ASME 2023 42nd International Conference on Ocean, Offshore and Arctic Engineering, OMAE 2023 held June 11-16, 2023, Melbourne, Australia with additional research and analysis. This paper is authored by Oluwatimilehin Mary Akindele, Judith Onyedikachi George, Dr. Abdelsalam Abugharara, and Dr. Stephen Butt.

3.1 Abstract

Large diameter drilling operations, including tunnel boring and raise boring, are capital-intensive projects. As such, proper estimation of time and cost is critical to the planning of the drilling project. To arrive at the correct estimation of the drilling time during the drilling phase, accurate prediction of the drilling performance is needed. In large diameter applications, disc cutters are the primary cutting tools, hence, several investigations have focused on developing accurate estimation of disc cutter forces. Other studies have also sought to understand the impact of rotary speed and cutter geometry on drilling performance. This study seeks to contribute to existing body of knowledge by evaluating the impact of cuttings cleaning efficiency on disc cutter drilling performance. This technical paper presents the results of two sets of drilling experiments. Both experiments were conducted under atmospheric conditions on the same granite block using the same rotary cutting machine and tri-disc disc cutter with tungsten carbide inserts. The same drilling parameters were applied during each of these experiments. However, the difference lies in the adopted cuttings evacuation method. One drilling procedure adopted the dry method wherein the cuttings were evacuated with vacuum while in the second procedure, the cuttings were

cleaned using the jetting action of a high-pressure spray nozzle. The results of these experiments show how much influence the cleaning efficiency has on the disc cutter drilling performance.

3.2 Introduction

There are three significant kinds of mechanical drilling - rotary drilling, sonic drilling, and rotary percussion drilling. A static WOB is applied to the rock in rotary drilling alongside the rotary drilling's planned rotary speed and flow rate. Rotary Drilling finds wide application in the following areas: Oil and Gas Drilling, Surface Mine Blasthole Drilling, Diamond Core Drilling, and Large Diameter Drilling (with Tunnel Boring Machine, TBM, and Raise Boring Machine). While the standard Oil and Gas drilling bit sizes range from 6 inches (152.4mm) to 28 inches (711.2mm) [57], the diameter of the drilled holes under Large Diameter Drilling is in magnitude of meters.

Large Diameter Drilling finds applications in mining, energy, marine, and construction [58,59]. Given these large diameter drilling applications, operators can drill both soft and hard formations. Some solids' mineral mining activities may involve drilling large diameter holes into quartz veins (quartz, a crystalline mineral) known to have an absolute hardness of ~7-7.5 on the Mohs' hardness scale [60]. Disc cutters are the dominantly used cutting tools on large diameter drilling machines (TBM or RBM).

Rock excavation performance optimization remains a concern despite the hole drilled or the rock (or soil) excavated. Rock excavation cost makes a significant contribution to the project cost. Amado indicated that in 2010, it could cost 55-88million USD to drill one offshore exploration or appraisal Oil and Gas well [61]. Drilling a hole necessitates the use of hydraulics to clean out the cuttings. Drill cuttings removal is critical during drilling to ensure drilling depth and efficiency. It cannot be over-emphasized how crucial it is to have a good understanding of wellbore hydraulics

during drilling [62]. The case is not different in a large diameter drilling operation. To prepare a realistic project cost and time estimate, the operator estimates the performance of the mechanical excavator during the project planning phase. An accurate understanding of the impact of cuttings cleaning on disc cutter drilling performance ensures that the rock excavation project will have reduced costs and time overruns. Avoiding cost overruns is especially important given the high capital costs that are associated with rock excavation.

Many investigators have studied hole cleaning in relation to how it impacts drilling rate with depth. Maurer [63] evaluated the effect of cuttings cleaning on ROP as seen in Figure 3-1 below. In his study, ROP varied directly with the rotary speed and to the square of WOB. It also varied inversely to the bit diameter squared and the square of the strength of the rock being drilled. Maurer [63] suggested that the condition where all of the rock debris is removed between tooth impacts indicates perfect cleaning.

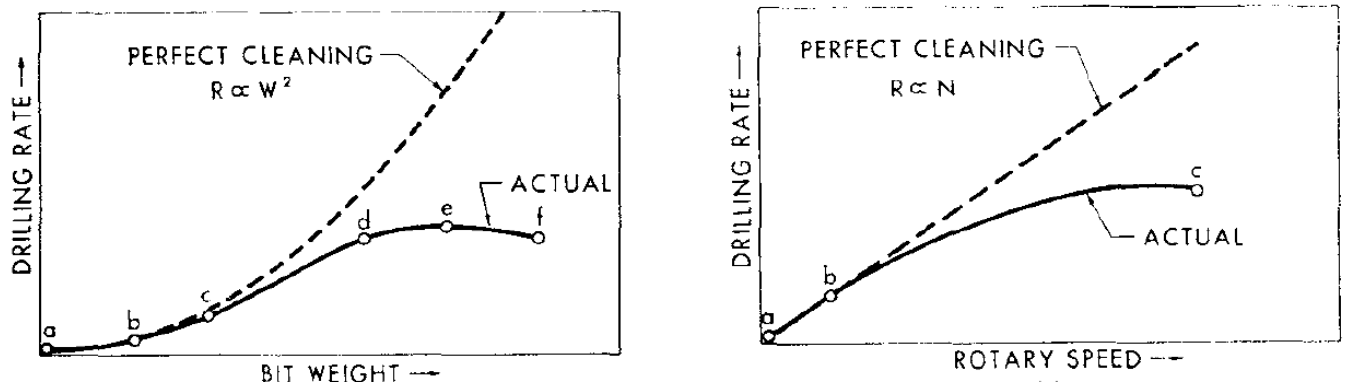

Figure 3-1: Maurer's [63] study on ROP-WOB-speed relationships

3.3 Materials and Methods

3.3.1 Drilling System

The Drilling Technology Laboratory (DTL) at Newfoundland has a Large Drilling Simulator (LDS) in place to conduct different drill-off tests using a Disc Cutter. The Large Drilling Simulator

provides the rotary torque and WOB for the drill-off tests. Up to 40KN WOB could be applied with the LDS. The torque limit of this system is 1100Nm, while the limit of the rotary speed is 1000rpm. The LDS simulates actual rotary drilling operations.

The LDS has five major integrated systems [64]:

- Power System
- Hoisting System: consists of two pneumatic cylinders, a hydraulic servo-actuator, one load cell, accelerometers, and magnetostrictive displacement transducers. This system applied the WOB required for drilling and measured the axial displacement.
- Rotary System: high torque motor
- Pumping System – water was circulated through the pumping system of the LDS in order to clean out the cuttings. Figure 3-2 shows the LDS system.
- Data Input and Acquisition (DAQ) System: With the LabView Manager integrated into the LDS, drilling parameters (WOB and Rotary Speed) were inputted into the LDS. Conversely, the measured data of the drill-off tests were obtained through the Data Acquisition System.

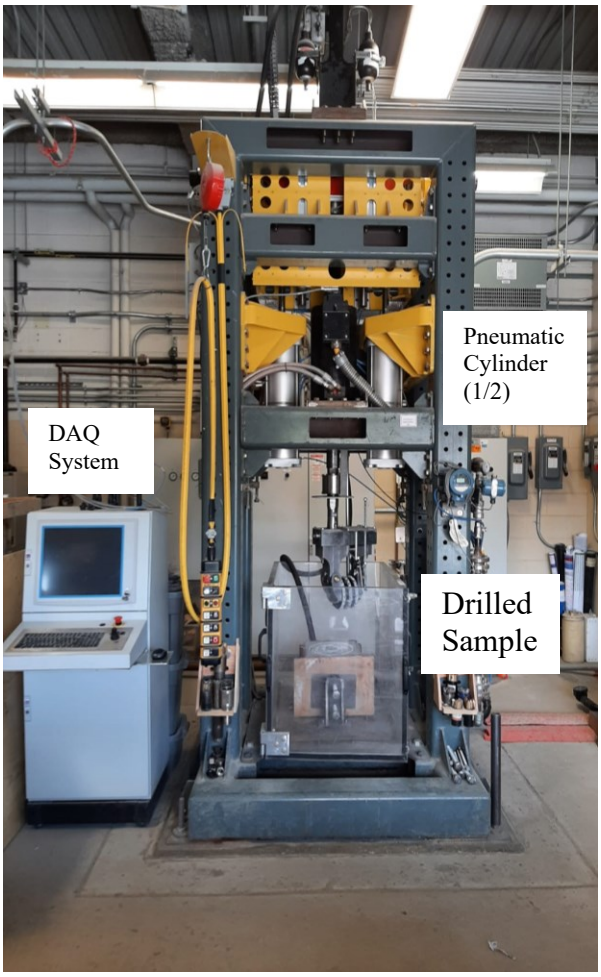

Figure 3-2: Large drilling simulator

3.3.2 Cutting Tool (Disc Cutter)

The cutting tool used for the experiment is a cylindrical triple-disc cutter (shown in Figure 3-3 below) with a pressure compensator with the following features shown in Table 3-1 below.

Table 3-1:Overview of the disc cutter used

S/N	**Overview**	
1	Number of Discs	3 (in an integral body)
2	Diameter	180mm
3	Cutter Type	Tungsten Carbide Inserts in a Matrix Body
4	Height of insert	5mm
5	Max Allowable WOB	69.9KN

Figure 3-3: Cylindrical disc cutter

3.3.3 Rock Sample

The rock sample is a plutonic igneous rock that is hard and brittle [29,65]. It is a coarse-grained igneous rock that consists mainly of anorthite, actinolite, muscovite, and quartz. Before these drill-off tests, an investigator with the DTL carried out an X-ray Diffraction Analysis on core samples [66]. This X-ray Diffraction analysis is complementary to the suite of tests carried out as part of the material characterization of designated rocks. Table 3-2 shows the mechanical properties of the drilled rock.

Table 3-2: Compositional analysis and mechanical properties of rock sample

Property	Number of Samples Tested	Mean	Standard Deviation
ρ_b (kg/m^3)	24	2900.63	34.46
UCS (MPa)	7	168.40	7.54
E (GPa)	7	13.31	2.31
V_p (m/s)	5	5480.91	109.34
ν_s (m/s)	5	3433.19	53.97
E′ (GPa)	5	81.14	1.43
ν	5	0.18	0.03
σ_t (MPa)	14	16.27	2.56
σ_{PLI} (MPa)	20	14.17	0.69
CAI	5	4.16	0.47
Mineral Composition	Anorthite (61.4%), Actinolite (22.4%), Muscovite (13%) and Quartz (3.2%)		

3.3.4 Cuttings Evacuation Techniques

For this study, the objective is to investigate how different cuttings cleaning methods impact the disc cutter drilling performance. As such, the same rock sample and the drilling setup were used for each drill-off test. The two main methods utilized for cuttings cleaning and removal include (i) Dry Cleaning (ii) Wet cleaning.

3.3.4.1 Wet Drilling Method

In the wet drilling setup, two flat high-pressure spray nozzles (Figure 3-4) were used to clean the cuttings generated under the disc cutter. Fresh tap water at atmospheric pressure was circulated through the LDS pumping system to remove the cuttings. Table 3-3 below shows the spray nozzles' specifications.

Table 3-3: Spray nozzles' specification

	Spray Nozzle 1	**Spray Nozzle 2**
Part Number	3234K996	3234K979
Angle (Degrees)	15	15
Connection	$\frac{1}{4}$ NPT Male	$\frac{1}{4}$ NPT Male
Max Flow Rate (gpm)	13.7	11
Max Pressure (psi)	300	300

Figure 3-4: Installed high-pressure spray nozzle

3.3.4.2 Dry Drilling Method

For dry drilling setup, a vacuum system was utilized for cuttings evacuation. Thus, no drilling fluid was circulated in the dry drilling run. The crushed rock cuttings were vacuumed out of the rock surface using a 16US Gallon 6.5HP Vacuum cleaner with a 20.53m length hose (Figure 3-5 below). This method of evacuation was assessed to carry some risk especially when experiencing increased vibration while drilling at increasing WOB values.

Figure 3-5: A 16US gallon 6.5HP vacuum cleaner for cuttings evacuation

3.3.4 Drilling Matrix

The drilling matrix for each drill-off test is shown in Table 3-4 below.

Table 3-4: Drilling matrix

Offset Distance (cm)	Applied Rotary Speed (rpm)	Applied WOB (KN)	Water Flowrate for Wet Drilling (litre/min)
6	10.0	7.2	11.5
		10.0	
		12.1	
		14.6	
		17.0	

For both sets of experiments (wet and dry drilling), the drilling setup and the drilled rock were the same. As the only varied aspect is the cleaning mode, the applied drilling parameters were kept the same too. Both drill-off tests were carried out at a constant rotary speed while varying the applied WOB. The offset distance of the disc cutter from the center of drill string rotation is 6cm.

3.4 Results and Discussion

As drilling progressed, the drilling data were recorded by the Data Acquisition System at a sampling frequency of 100Hz. As such, a significant quantity of data was collected and analyzed in order to understand the drilling performance for each drilling run. The output drilling data included vertical displacement, time, and drilling torque. The recorded data also showed the bit-rock interactions, confirming the applied rotary speed, WOB, and presence or absence of drilling vibrations. Two major indicators, the rate of drilling penetration and drilling torque, were used to evaluate the drilling performance for each adopted mode of cuttings cleaning. The drilling penetration rate is the slope of the plot of the recorded vertical displacement (when the disc cutter is on bottom) against the cumulative drilling time. A sample plot is shown in Figure 3-6 below. The plot indicates a general upward increase in vertical displacement as drilling progressed. The rate of penetration in the plot below is 0.0385cm/min. The solid line represents an approximated linear line of best fit while the upper dash line and lower dash line show the data's upper and lower boundary, respectively.

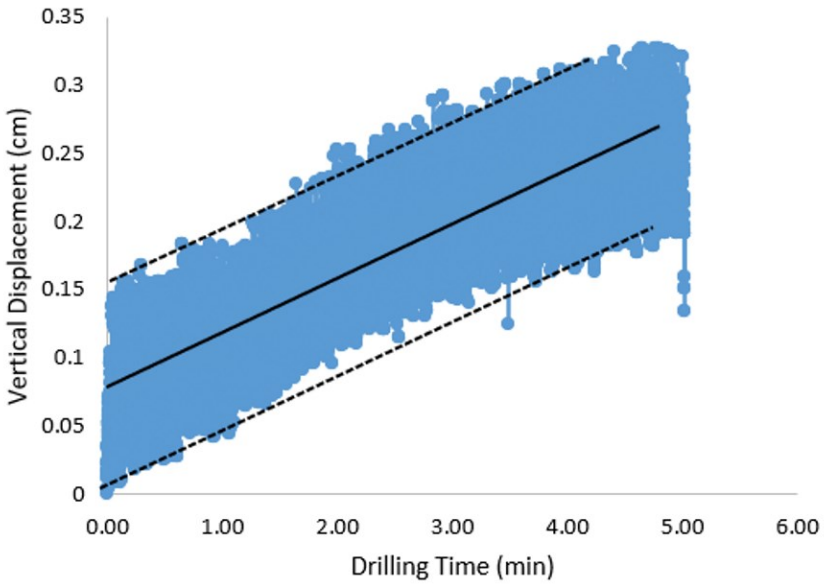

Figure 3-6: Displacement-time plot (17.0KN, 10RPM)

Figure 3-7 shows the drill-off test results for both cuttings cleaning modes. From Figure 3-7, the ROP increased with increasing WOB for wet drilling. One key feature of wet drilling is the cooling effect of the water on the cutting tool. In addition, the jetting water flushed the rock cuttings completely away from the rock surface, enabling the disc cutter to engage a fresh rock face.

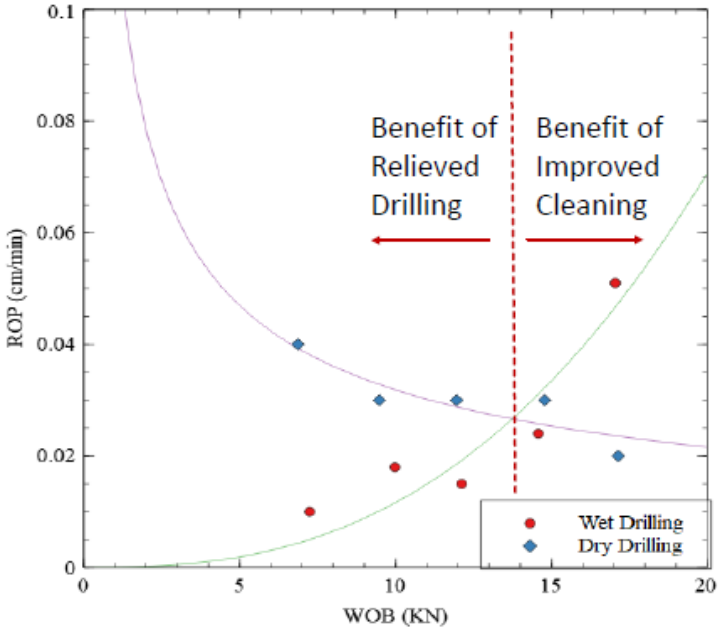

Figure 3-7: ROP vs WOB (wet drilling and dry drilling)

The drilling torque for each applied drilling parameter was recorded. The average drilling torque was computed for each drilling step. Also, the standard deviation was computed to evaluate the variability of the collated data. Increased drilling torque indicates better rock-cutter interaction as is shown by Maurer [63] in Equations 3-1 (for perfect cleaning) and 3-2 (for poorer cleaning).

$$T \propto WOB^2 \qquad (3\text{-}1)$$

$$T \propto WOB^{1.5} \qquad (3\text{-}2)$$

Figure 3-8 shows the plot of the average recorded torque for the wet and dry drilling. From Figure 3-8, it can be seen that the drilling torque for wet drilling was always higher than the drilling torque

for dry drilling at the lower WOB values. This indicates that there is more bit-rock interaction due to better cuttings evacuation.

Thus, Figures 3-7 and 3-8 show a clear distinction between the drilling performance during wet drilling and that of dry drilling. The drilling performance (rate of penetration and drilling torque) increased with improved cleaning, especially at increased WOB levels (where there is often the existence of higher disc cutter vibrations).

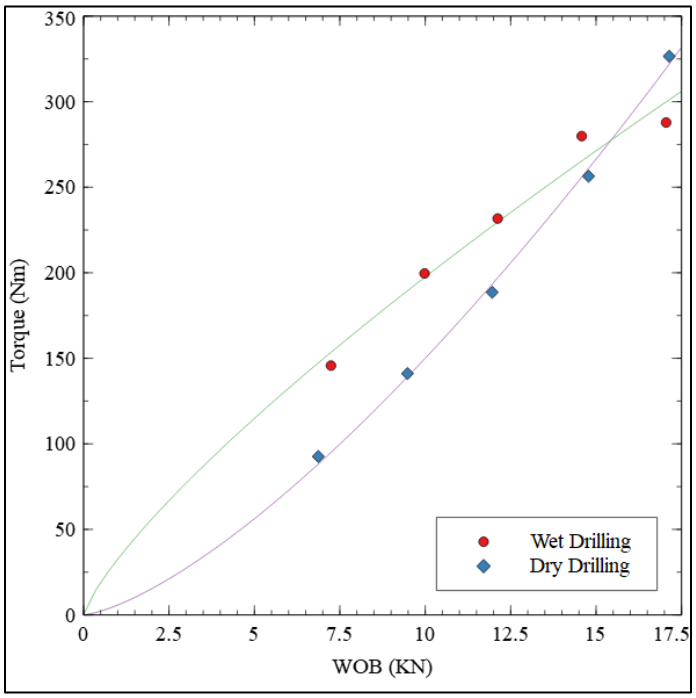

Figure 3-8: Torque vs WOB (wet drilling and dry drilling)

From the cuttings size analysis, wet drilling in almost all cases had larger cuttings size unlike dry drilling implying a more efficient cuttings removal (perfect cleaning) until the highest WOB. The cuttings size for both cleaning method get progressively smaller with increasing WOB as seen in Table 3-5 which could be because of possible reduction in cleaning efficiency or regrinding for both methods. Figure 3-9 shows the graphical presentation of the cuttings size distribution for wet and dry drilling method.

Table 3-5: Cuttings size distribution at different WOB for both wet and dry drilling

Dry Drilling						
WOB (KN)	D10 (mm)	D30 (mm)	D50 (mm)	D60 (mm)	D80 (mm)	D90 (mm)
7.2	< 0.075	0.095	0.125	0.366	0.480	0.540
12.1	< 0.075	0.082	0.175	0.246	0.430	>0.6
14.6	< 0.075	0.086	0.153	0.223	>0.6	>0.6
17.2	0.092	0.138	0.290	0.437	>0.6	>0.6
Wet Drilling						
	D10 (mm)	D30 (mm)	D50 (mm)	D60 (mm)	D80 (mm)	D90 (mm)
7.2	0.080	0.136	0.228	0.313	1.080	1.746
12.1	0.075	0.112	0.173	0.227	0.577	1.532
14.6	< 0.075	0.114	0.182	0.236	0.445	1.549
17.2	0.089	0.183	0.229	0.251	0.536	2.022

A

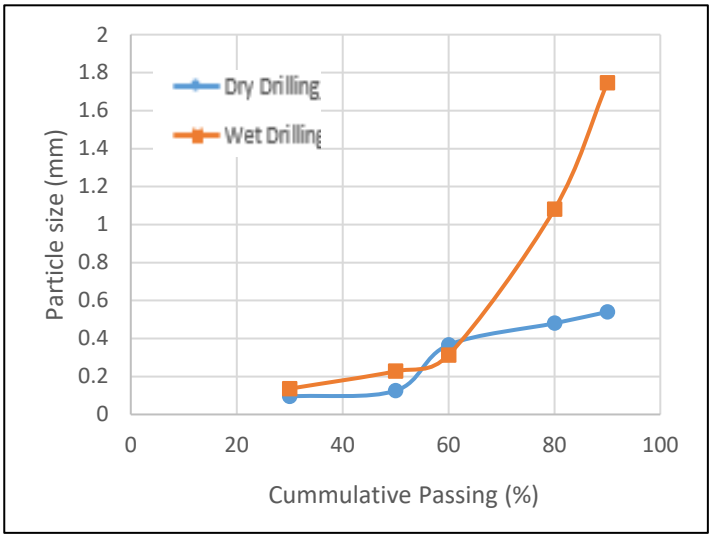

B

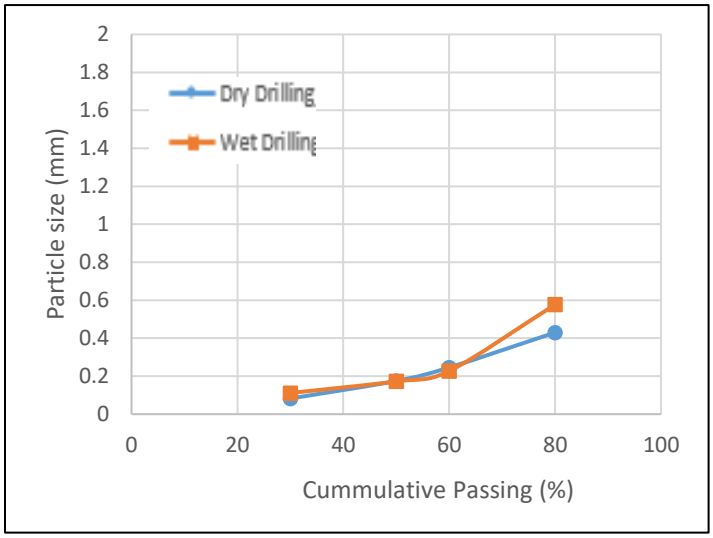

C

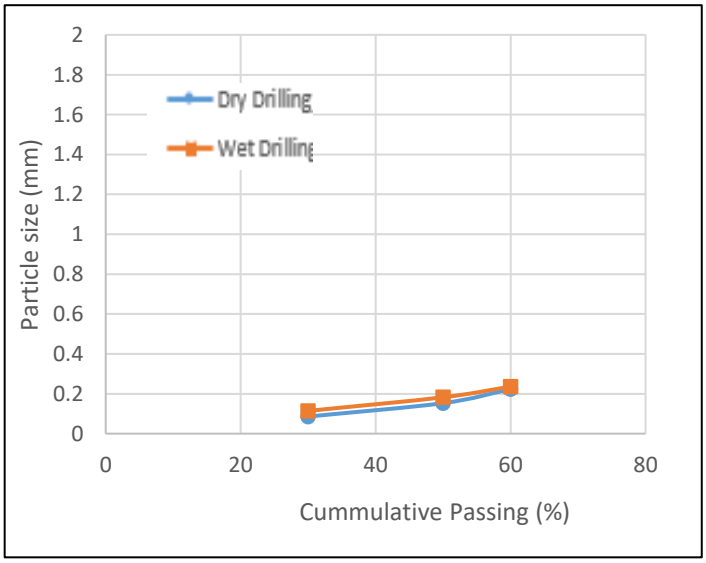

D

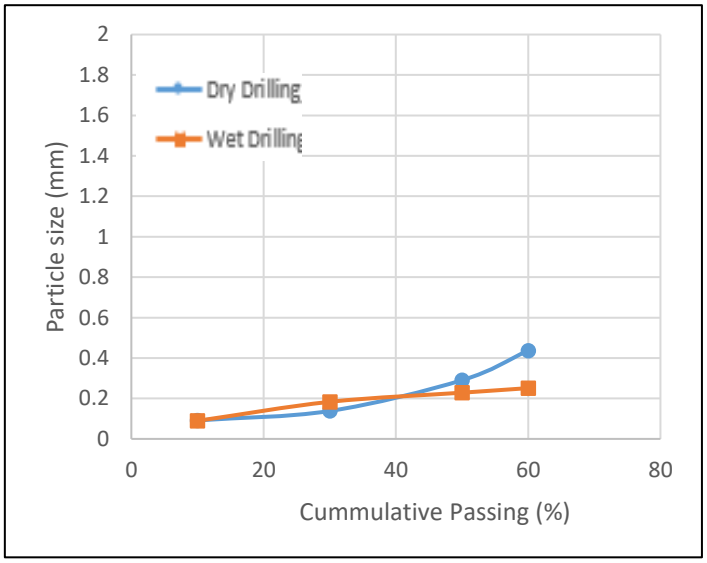

Figure 3-9: Cuttings size distribution at (A) WOB of 7.2 KN (B) WOB of 12.1 KN (C) WOB of 14.6 KN (D) WOB of 17.2 KN

3.5 Conclusion

This technical paper has explored the impact of cleaning efficiency on drilling performance. The drilling system, rock properties, cutting tool features, and different cleaning modes have been presented. The results of each set of drill-off tests were analyzed. These results show that there are observed relationships between the drilling performance and the adopted cleaning efficiency. For

the same applied WOB and rotary speed, the drilling performance (rate of penetration, drilling torque, and cuttings size distribution) was higher for the wet drilling setup. This is an indication of better cuttings cleaning by the wet drilling method. This is completely in alignment with the expectation from literature. One key source that had been previously cited (Maurer, 1962) explains that for the same set of input WOB (at constant rotary speed), the drilling rate and drilling torque increase with perfect cleaning.

4. Volume Estimation for Unrelieved Mode of Cutting

This chapter discusses the different available options for volume estimation of excavated cuttings for unrelieved cutting mode done in a laboratory setting. It is written to be submitted as a technical note in a journal for volume estimation experimental methods. This note is authored by Oluwatimilehin Mary Akindele, Dr. Abdelsalam Abugharara, and Dr. Stephen Butt.

4.1 Abstract

To determine the efficiency of a drilling operation, a pivotal metric is the measurement of rock excavated volume, providing insights into the specific energy expended during the drilling process. Depending on the mechanism of rock failure (crushing and chipping) involved during a cutting process influenced by the drilling parameters, the mode of cutting can either be relieved or unrelieved. With an unrelieved cutting mode, it is, however, challenging to estimate the volume of rock surface removed per unit time. This study explores the utilization of a 3D scanner to evaluate the rock excavated volume during drilling. The findings demonstrate the application of the 3D scanner in capturing, analyzing, and interpreting cutter groove profiles from drilled block, enabling the precise measurement of rock chip volume essential for calculating its specific energy.

4.2 Introduction

Large diameter drilling by mechanical approach finds application in mining, energy, marine and construction with disc cutters as the predominant tool. Its application has increased significantly over the years, small-scale (core cutting) and full-scale laboratory rock cutting tests have become essential to provide fundamental data for cutter selection, design, and performance prediction for a particular rock formation [67–71]. This has drawn a lot of attention from researchers as it should be noted that the primary cause of rock failure is the interaction between the cutter and the rock,

and that the geometric shape of the contact body is a key determinant of the contact behavior. According to Liu et al. and Cao et al. [72-73], full-face tunnel boring machines (TBMs) have the advantages of great excavation efficiency, good safety, strong geological adaptation, and minimal environmental effect. The disc cutter which is the predominant tool used is located at the front of the TBM and is in direct contact with the rock mass. The cutter-rock contact behavior plays a major role in determining the rock-cutting efficiency of the TBM and the drilling progress. When a TBM is employed in hard rock stratum, the normal force needed for the cutter to penetrate a given depth into the rock increases rapidly as the uniaxial compressive strength of the rock increases [74-75]. Prediction of the rock excavation performance of large diameter drilling using disc cutter for any geological formation is one of the main concerns in determining the economics of the drilling operation as proper understanding of rock fragmentation mechanism is the foundation of efficient cutters selection, design, arrangement, and operation optimization.

Numerous in-depth studies have been conducted to provide useful information for the design and improvement of the rock-cutting ability of TBMs considering several factors involving the cutter structure and layout, drilling parameters, and the rock properties. The mechanism of failure of the rock under the disc cutter explains the pattern of cut obtained on the rock surface. There are two main mechanisms of rock failure: crushing (under each disc due to the applied compressive load) and tensile failure (chipping resulting from the connection of the cracks created and propagated between adjacent grooves). Crushing produces highly fractured, little rock fragments in the form of chips that resemble powder, whereas chipping starts and propagates fractures to produce large rock fragments, i.e., chunk-like rock chips [25].

The combined impact of these two mechanisms results in the removal of the complete exposed half-space of the rock. This mode of cutting is named relieved cutting as a uniform cross-sectional

area of rock is removed per unit time. To achieve relieved cutting, the rock properties (shear strength, compressive strength, rock quality designation), disc cutter geometry (including the angle at the tip) as well as the spacing between subsequent cuts play a significant role. Figure 4-1 below shows the interaction of groove for a relieved disc cutting mode and the cutter spacing required to achieve it [29,30].

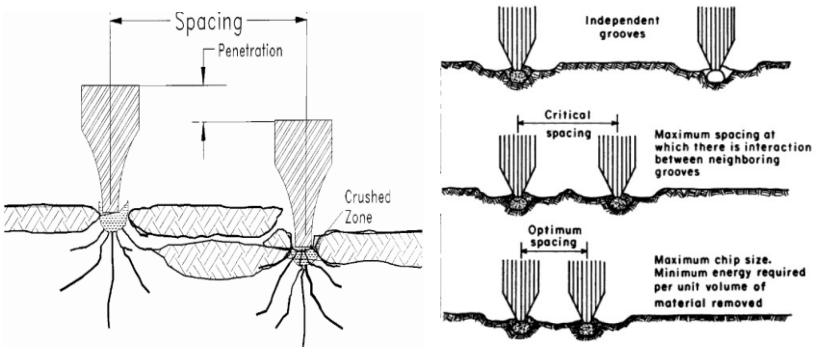

Figure 4-1: A) Relieved disc cutting mode - interactive grooves [29] B) Optimum and critical cutter spacing [30]

When the cutting of the rock is attributable to crushing under the discs as well as side forces due to cutting at tight radii, this pattern of cutting is called unrelieved cutting. It is often observed on high-strength intact rocks especially when the spacing between the discs is too high for the micro cracks to coalesce and propagate to the free surface [29].

In relieved cutting, a uniform cross-sectional area of rock is removed per unit time. Knowing the rate of penetration, the excavated volume of rock per unit time can therefore be computed. With unrelieved cutting however, it is especially challenging to estimate the volume of rock surface removed per unit time. Figure 4-2 shows an example of a specimen drilled in an unrelieved cutting mode. This work examines how a cutter groove profile of a drilled block profile can be scanned, analyzed, and interpreted for measuring rock chip volume needed to compute its specific energy.

A  B 

Figure 4-2: A) Fresh specimen for unrelieved drilling experiment B) Drilled specimen (Rock dimension: 30cm by 30cm by 16cm)

4.3 Volume Measurement Techniques

Six different approaches have been explored to determine the volume of rock excavated for a drilled block in the single disc cutter drilling experiments for unrelieved cutting mode, all are briefly explained in this section. However, this study focuses on the 3D scanning of drilled block to determine the excavated rock volume which will be explained in the materials and method section.

4.3.1 Rock Surface Measurement

This method involves the use of vernier calipers to measure the drilled depth and widths of grooves on the rock surfaces. In this case, the deepest drilled depth and the widest point on the groove are measured. This measurement method is a quick approximation, and it provides early insights. However, the measured dimensions do not capture the unique geometry of the drilled grooves and so it is not an accurate measurement of drilled rock volume that could be used for calculating Mechanical Specific Energy. This method is quite time-consuming and measurement of these dimensions under a suspended drill string posed a risk of finger crushing. Figure 4-3 shows the

rock surface measurements. Estimating the rock chip volume using the measured dimensions will involve mathematical integration which is not straightforward.

Figure 4-3: Rock surface measurements

4.3.2 Laser Scanning

This method involves the use of laser scanner as seen in Figure 4-4 below, a non-contact device to capture discrete data points using laser infrared technology producing detailed 3D images. The scanner head turns, sweeping the laser across the object. The geometry needed to interpret the laser's route into 3D data is provided by objects in its path by reflecting the laser beam back to the scanner.

Laser scan helps in obtaining an accurate rock volume groove measurement. However, this method does not allow for intermittent capturing of rock surface in the large diameter drilling simulator as drilling progresses. This is because it involves manual handling of the heavy rock sample for each scan and so the scan could only be carried out at the end of the drilling run and not for drilling progress monitoring.

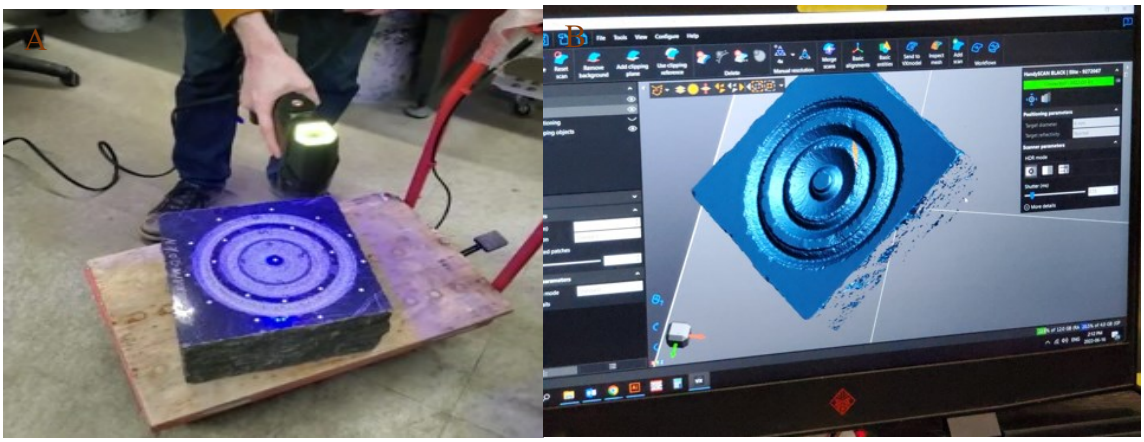

Figure 4-4: (A) Laser scanning process (B) 3D Laser scan of the Granite surface

4.3.3 Cuttings Mass Measurement

This method involves measuring the mass of the cuttings produced during drilling, and then calculating the volume of rock excavated using the measured cutting mass and rock density. While this method seems easy to do, it is not a technique to give an accurate result as it doesn't account for cuttings lost during cleaning/ cuttings evacuation especially when the cuttings size are small.

4.3.4 Use of Fine Sand

This method involves the use of dry fine sand to determine the volume of cuttings excavated. A known volume of sand is poured into a beaker and poured into the vacuum created on the rock to fill it up as seen in Figure 4-5. The volume of sand poured into the empty space created by the experimental drilling operation signifies the volume of cuttings excavated from the rock. This is calculated by subtracting the volume of sand left in the beaker from the initial measurement of sand poured into the beaker. While this method might seem easy, it is necessary to take extra care while handling the fine sand due to dust that might be introduced.

Figure 4-5: Rock groove filled with fine sand for drilled cuttings volume estimation (Rock dimension: 45cm by 45cm by 45cm)

4.3.5 2D Scanning

This method involves the use of a Contour gauge also known as a profile gauge; a measuring device used to capture the cross-sectional shape of the rock surface. It consists of several plastic or steel pins set against each other in a frame shown in Figure 4-6 below. The frame keeps the pins parallel in the same plane and the movement of each pin is independent of the others and perpendicular to the plane. By profiling the surfaces, it is simple to compare them to one another or to a standard profile to see if any material has been lost because of corrosion or other reasons. The gauge is placed in a quadrant as seen below to replicate the profile, then the profile is carefully traced on a standardized graph sheet and interpreted/ analyzed using a graph reader. This method is prone to a lot of human errors.

Figure 4-6: Contour gauge used for groove mapping

4.3.6 3D Rock Groove Scanning

The 3-D Scanning method which involves the use of a 3D scanner is used to produce a 3-D Scan of the rock surface and can be done at different phases of the disc cutter drilling experiment without moving the rock sample away from the large drilling simulator to monitor drilling progress and at the end of the drilling operation. In combination with appropriate CAD software like Solidworks, the 3D-Scan can be used to compute the rock groove volumes and drilled depths.

4.4 Materials and Methods

4.4.1 Rock Sample

Rock sample is a plutonic igneous rock that is hard and brittle [29,65]. It is a coarse-grained igneous rock that consists mainly of anorthite, actinolite, muscovite, and quartz. Before these drill-off tests, an investigator with the DTL carried out X-ray Diffraction Analysis on a granite core sample [66]. This X-ray Diffraction analysis is complementary to the suite of tests carried out as part of the material characterization of designated rocks. Table 4-1 shows the mechanical properties of the drilled granite rock.

Table 4-1: Compositional analysis and mechanical properties of rock sample

Property	**Number of Samples Tested**	**Mean**	**Standard Deviation**
ρ_b (kg/m^3)	24	2900.63	34.46
UCS (MPa)	7	168.40	7.54
E (GPa)	7	13.31	2.31
V_p (m/s)	5	5480.91	109.34
ν_s (m/s)	5	3433.19	53.97
E′ (GPa)	5	81.14	1.43
ν	5	0.18	0.03
σ_t (MPa)	14	16.27	2.56
σ_{PLI} (MPa)	20	14.17	0.69
CAI	5	4.16	0.47
Mineral Composition	Anorthite (61.4%), Actinolite (22.4%), Muscovite (13%) and Quartz (3.2%)		

4.4.2 Disc Cutter

This is the cutting tool used for the laboratory experiment to drill the rocks scanned for determining its excavated volume. It is a cylindrical triple-disc cutter (Figure 4-7) with a pressure compensator and tungsten carbide inserts in a matrix body.

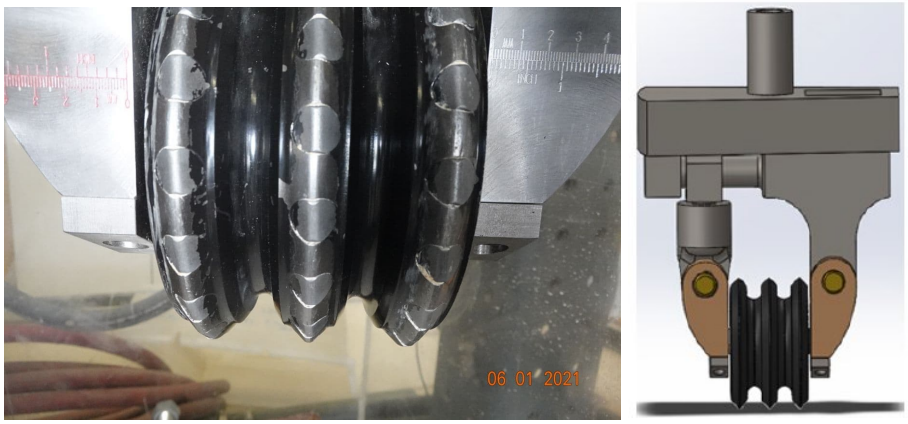

Figure 4-7: Cylindrical disc cutter

4.4.3 3D Scanner

The 3D scanner used in this study as shown in Figure 4-8 below combines the most recent scientific research findings with the functions of a desktop and handheld 3D scanner. It uses a high-speed intelligent chip and 3D camera hardware, which improves performance and delivers precise depth data of rock grooves. With the aid of the patented micro-projecting chip and the binocular & micro-structured light principle, the scanner enables quick acquisition of high-accuracy (up to 0.1mm) 3D point cloud data of the rock surfaces. The scanner-integrated high-performance 3D calculation chip, which uses sophisticated algorithms, effectively ensures seamless scanning without freezing, even when it is utilized with a regular PC [76].

Figure 4-8: 3D scanner

4.4.4 Scanning the Rock Specimen

For Scanning the rock specimen to analyze the rock grooves and cuts, the “Marker” scanning method is the best way to follow. For Scanning the Grooves, the markers adhere to the specimen in random order for the scanner to differentiate different locations on the specimen. It is necessary to maintain the random order while sticking the markers and to stick as many markers as possible

for more precise scanning. A reference pointer can be glued on or drilled into the specimen for correct orientation, as seen in Figure 4-9.

Figure 4-9: Rock specimen with markers and reference hole

4.4.5 Analyzing the Scanned Specimen

Solidworks is used to analyze scanned specimens. It is a 3D CAD design, analysis, and product data management software. The software has a lot of capabilities, of which one of its functions is to help evaluate a solid volume (internal & external) using point cloud analysis. The image is uploaded into Solidworks as a surface body, and a reference plane is created on the image rock surface for analysis.

4.5 Results and Discussion

Using the 3D scanner, a 3D image of the rock groove created from a drilling experiment was captured and analyzed using Solidworks. Figure 4-10 shows the rock specimen with markers, a reference hole, and the scanned 3D image. The image is uploaded into Solidworks as a surface body with a reference plane and cylinder created on the imported image to capture the rock surface groove with a known diameter and height. The known diameter and height of the cylinder is used

to estimate the rock surface volume, while solidworks evaluate the rock surface body taking into consideration the groove on the rock surface. Figure 4-11 shows an analyzed rock surface on solidworks. The rock cuttings excavated is estimated as:

Rock cuttings excavated = Rock surface volume – Rock surface volume (groove inclusive)

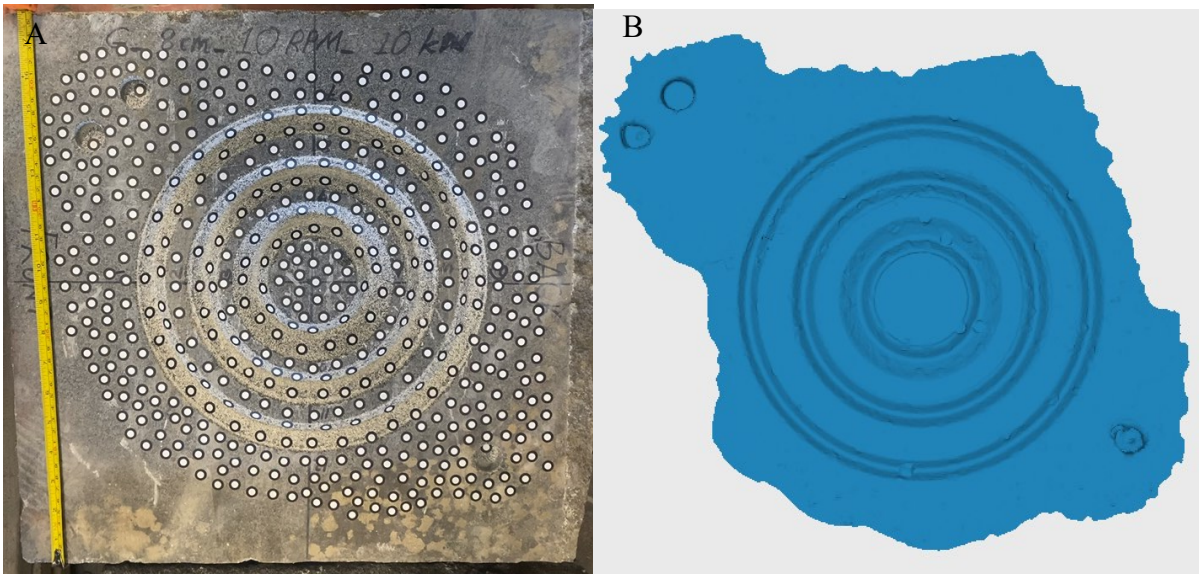

Figure 4-10: (A) Rock specimen with markers and reference holes (B) Scanned rock specimen showing the reference holes

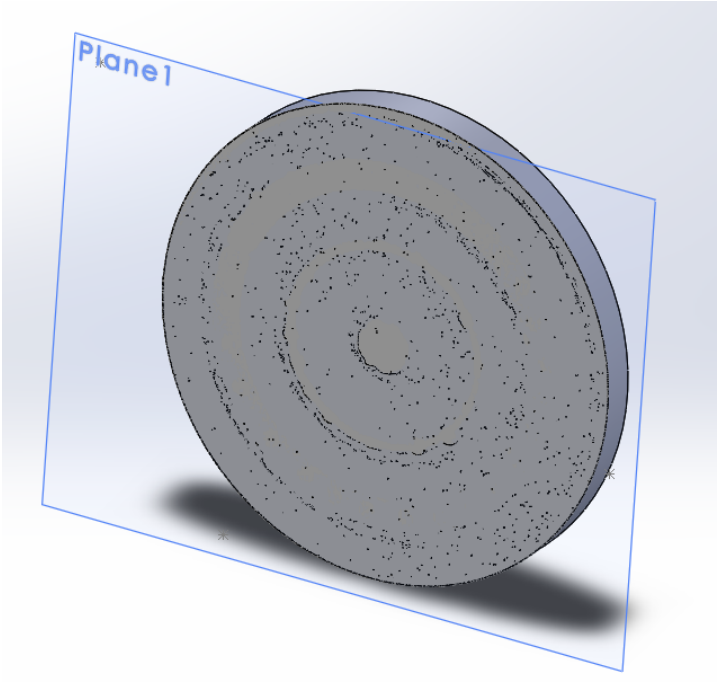

Figure 4-11: Analyzed rock surface on solidworks

Table 4-2: Table showing the result of solidworks analysis for volume estimation

WOB (KN)	Lateral Displacement (cm)	Depth of Groove (mm)	Total Volume (mm^3)
5	6	10.8	77762.60
		9.52	
		8.76	
	8	8.7	90308.03
		7.48	
		6.62	
	10	8.5	138958.3
		7.43	
		6.46	
12.5	10	10.45	192551.29
		9.63	
		8.25	
15	6	12	196152
		10.7	
		9.65	
		10.69	
		9.53	

Lateral displacement represented in Table 4-2 is the position of the middle disc of the cylindrical disc cutter during the drilling experiment with respect to the center of drillstring rotation.

4.5.1 3D Excavated Volume Validation

3D scanning method and analysis using solidwork was validated using the dry fine sand method for rock cuttings volume. This was done for rock groove drilled at 5 KN, 8 cm lateral displacement and 15KN, 6 cm lateral displacement. The result of this analysis is presented in Table 4-3 below.

Table 4-3: Results of 3D scanning method in comparison with dry fine sand method

WOB (KN)	Lateral Displacement (cm)	3D Scan Cuttings Volume (mm^3)	Dry Fine Sand Cuttings Volume (mm^3)	% Difference
5	8	90308.03	91000	0.76
15	6	196152	195000	0.59

The percentage difference between the 3D scan method and the dry fine sand method was estimated to be less than 1%. This method gives a fairly consistent value for rock volume

estimation, validating the 3D scanning method overcoming the dust challenge while using the dry fine sand method.

This study confirms the effectiveness of the 3D scanner in determining the volume of rock excavated for an unrelieved cutting mode of drilling operation. One shortcoming noticed in the use of the 3D scanner is its ability to scan a rock with shining surface since its method of scanning is the marker method. The markers reflect into the scanner as data point, for a shining rock surface the scanner is not able to capture data point because of the rock surface's reflective nature.

4.6 Conclusion & Recommendation

In conclusion, this study has introduced a streamlined approach to calculating the volume of rock cuttings excavated and monitoring drilling progress within laboratory environments. The methodology presented herein holds promise for facilitating informed decision-making regarding drilling parameters, thereby contributing to greater efficiency in drilling operations. Through the implementation of this innovative technique, the research has taken a significant step towards enhancing the effectiveness and accuracy of drilling processes, laying the foundation for future advancements in drilling technology.

Moving forward, further exploration into alternative scanning methods for illuminated rock surfaces represents a key avenue for future research. By continuing to refine and expand upon the techniques introduced in this study, there exists the potential to unlock even greater insights into drilling operations and optimize drilling processes to a greater extent.

5. Effect of Preparation Method and Weighting Agent Particle Size on Imaging Fluid Quality and Rheological Properties

This chapter discusses a technical paper scheduled to be published with ARMA Golden 2024 conference. The authors of this paper are Leila Abbasian, Oluwatimilehin Mary Akindele, Dr. Abdelsalam Abugharara, and Dr. Stephen Butt. The paper has been submitted and accepted.

5.1 Abstract

Imaging fluids plays a crucial role in mitigating the impact of borehole groundwater on borehole Ground Penetrating Radar (GPR) results. Such fluid possesses specific characteristics such as low conductivity to minimize electromagnetic wave attenuation, appropriate dielectric permittivity to prevent signal ringing at the fluid-wellbore boundary, higher density than water for settlement at the bottom hole, and long-term stability throughout the imaging process. This study examines the influence of agitation and temperature on the quality of oil-based imaging fluids, comparing two major preparation methods with distinct grain sizes of the weighting agent. One is the conventional method involving a critical heating step of the emulsifier in 20% of the imaging fluid liquid base, while the second involves dissolving the emulsifier in the liquid base by agitation. Evaluation of the produced fluids encompasses considerations of their stability over time, settlement in various water temperatures, and rheological properties. The results of these experiments reveal the effect of agitation, weighting agent grain size, and temperature on the overall quality of the produced imaging fluid.

5.2 Introduction

Electromagnetic waves are used as the source of Ground Penetrating Radar (GPR) to image underground structures [52]. Borehole GPR utilizes high frequency electromagnetic waves for

mapping out the downhole subsurface geology. This GPR data quality and penetration can be influenced by the presence of borehole water or the media between the antenna and the wellbore [77]. Hence, the selection of a proper borehole fluid will help overcome the impact of ground water on imaging data quality. Borehole water should be replaced by an imaging fluid at the bottom hole and cover the E-M antennas while imaging.

The ideal borehole fluid (imaging fluid) should have specific properties such as low conductivity (low EM wave attenuation), appropriate dielectric permittivity close to that of the host rock to avoid signal ringing between the fluid-wellbore boundary, higher density than water to enable it settle at the bottom hole, and stability such that it does not discompose while imaging. Following the above characteristics, the imaging fluid is made up of a fluid base with low dielectric permittivity and conductivity, a weighting agent to increase imaging fluid density more than that of water, and an emulsifier to ensure its stability by preventing the separation and settlement of suspended solids.

Research has been done to come up with a distinct recipe for the imaging fluid meeting all necessary characteristics and conditions as mentioned above. This study sought to modify the developed standard of preparation of the imaging fluid by eliminating the preheating step of the emulsifier and investigate its impact on the imaging fluid quality and rheological properties.

5.3 Rheological Properties of Fluids

Rheology is the study of the deformation and flow of matter. It is possible to predict how a fluid will flow under various variables, such as temperature, pressure, and shear rate, by taking specific measurements of the fluid. Some of the rheological properties studied in this study are as follows [2]:

- **Plastic viscosity (PV)**, a measurement of the fluid internal resistance to flow because of solids interaction in a fluid, primarily by the mechanical friction between the suspended solid particles, the solid particles, and the liquid phase. Plastic viscosity is expressed in centipoise (cP) and can be estimated as the difference between the 600rpm and the 300rpm viscometer dial readings.

$$\mu_p = \theta_{600} - \theta_{300} \qquad (5\text{-}1)$$

The following are the main determinants of fluid plastic viscosity:

  - Solids concentration.
  - Size and shape of solid particles present in the fluid.
  - Viscosity of the fluid phase.
  - The presence of some long-chain polymers.
  - Oil-to-Water or Synthetic-to-Water ratio in invert-emulsion fluids.
  - Type of emulsifiers in invert emulsion fluids.

- **Yield Point (YP)** is a measure of the electrochemical or attractive force in a fluid under flow conditions. It is the measure of the fluid internal resistance to initial flow; it is that part of the resistance to flow that may be controlled by proper chemical treatment [78]. The yield point will decrease as the attractive forces are weakened by chemical treatment. Mathematically, it is expressed as

$$YP = \theta_{300} - PV \qquad (5\text{-}2)$$

  The unit is lbm/100ft^2 or Pa.s.

  Yield point can be affected by the following factors [78,79]:

  - Surface properties of the fluid solids
  - Volume concentration of the solids
  - Concentration and types of ions in the fluid phase

- **The ratio of YP/PV** is a significant indicator of a fluid condition. It is a measure of the shear thinning behavior of drilling fluids. A high ratio means the fluid is more shear thinning (viscosity decreases under shear strain). Low ratios indicate a greater settling velocity of solids.
- **Apparent Viscosity** is the viscosity of a drilling fluid at a specific shear rate and constant temperature. The relationship depends on the fluid's yield point and plastic viscosity, it is expressed in centipoise (cp) [80]. It is also known as the effective viscosity and expressed as;

$$\mu_a = \frac{\theta_{600}}{2} \qquad (5\text{-}3)$$

Where θ_{600}= Viscometer dial reading at 600 rpm

- **Filtration rate**: This gives an idea on the amount of mud filtrate invasion into porous and permeable formation and the amount of filter cake that will be deposited on the wall of the wellbore whenever filtration happens. As fluid is lost, mud solids begin to build up on the face of the wellbore. This is the filter cake.
- **Flow Behavior Index (n):** This is an indicator of the tendency of a fluid to shear thin and it is dimensionless. When n < 1, the fluid experiences shear thinning and when n > 1, the fluid experiences shear thickening. Shear thinning fluids decrease in viscosity as stress increases, while shear thickening fluids increase in viscosity with increasing stress.

$$n = 3.32log(\frac{\theta_{600}}{\theta_{300}}) \qquad (5\text{-}4)$$

Where θ_{600}= Viscometer dial reading at 600 rpm and θ_{300}= Viscometer dial reading at 300 rpm

- **Consistency Index Factor (K):** This is defined as the viscosity index of the fluid system and the unit is lb/100ft2. It is the measure of a fluid change in viscosity with temperature change.

$$k = \frac{\tau}{\gamma^n} = \frac{\theta_{600}}{1022^n} \qquad (5\text{-}5)$$

5.4 Materials and Methods

5.4.1 Basic Ingredients and General Protocol

The three ingredients used to prepare the imaging fluid are described below.

- Fluid base: Canola oil with a dielectric constant of 2.
- Weighting agent: Barite to increase the density of the mixture to 1.2g/cc, allowing for the settlement of the imaging fluid downhole. In this study, two different kinds of barite based on its particle size were used. API barite (d50 of 40μm) and Microbarite (d50 of 2-6μm).
- Emulsifier: Stearic acid which serves as the gelling agent for the imaging fluid to maintain stability with dielectric constant of 2.

The general protocol to prepare the imaging fluid is described below.

- Measure all ingredients (Canola oil, Barite, and Stearic acid).
- Melt the stearic acid by heating it up in 20% of the canola oil to 100°C, until the stearic acid totally melts.
- Put the remaining 80% of canola oil in a bucket and add the dissolved mixture. Mix the oil until it is clear without any wax.
- Add barite into the dissolved mixture. Barite should be added using a sieve to slow down the process and to separate the barite powder. Mix the mixture while adding barite.
- Mix for 10 minutes.

5.4.2 Dissolving Stearic Acid

To investigate an alternative to the heating process of dissolving stearic acid in canola oil and its effect on the quality of the imaging fluid prepared, 3 different imaging fluid procedures were used

for the same quantity of API barite and Microbarite. A total of 6 imaging fluids were prepared with its breakdown below.

- Dissolving stearic acid by agitation using a mixer with 3000rpm and adding barite at high temperature.
- Dissolving stearic acid by agitation using a mixer with 3000rpm and adding barite at low temperature. Note: Before adding API barite in this method, the stearic acid and canola mixture was beginning to solidify and so all of it was oven heated and cooled to a low temperature.
- Dissolving stearic acid by heating in 20% liquid base (general protocol)

Figure 5-1 below shows the hand drill mixer (3000rpm) and the experimental setup for the agitation process in dissolving stearic acid in canola oil and for mixing barite in the dissolved stearic acid and canola oil mixture. Figure 5-2 shows the oven used for heating up and dissolving stearic acid in canola oil.

Figure 5-1: Hand drill mixing blade and experimental setup

Figure 5-2: Oven used for heating and dissolving stearic acid

5.5.3 Imaging Fluid Quality Check

To evaluate the quality of the imaging fluid produced, its stability over time was observed, settlement in different water temperatures was confirmed, and its rheological properties were measured. It is desired that when the produced imaging fluid is set aside and behavior monitored over time, it remains stable and does not separate. It is also desirable that imaging fluid when poured into water of temperatures 5°C and 24°C, it remains settled in the water.

5.5.4 Rheological Property Measurement

For this study, two major pieces of equipment shown in Figure 5-3 below were used to determine the rheological properties of the imaging fluid. One is the direct indicating viscometer (an OFITE 8-speed rotational viscometer) used to determine the rheological characteristics of the fluid at atmospheric pressure (14.7 psi), and a Filter Press for fluid loss (filtration) test.

A

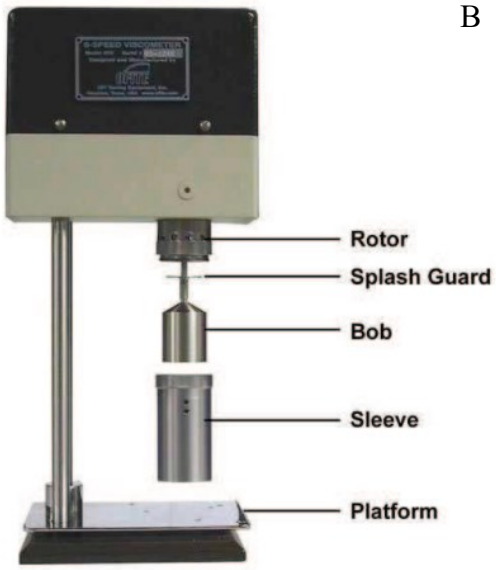

B

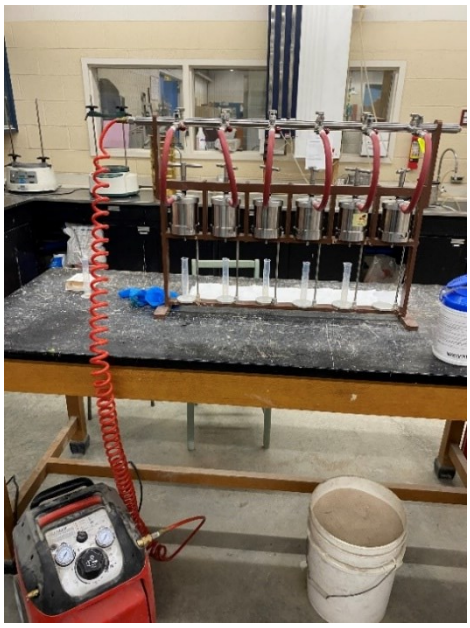

Figure 5-3: (A) OFITE 8-speed rotational viscometer (B) API fluid loss test kit

5.6 Results and Discussion

After the imaging fluid was prepared as described above, separation test, settlement test, and rheological property measurements were done. The results of the test are described below.

5.6.1 Separation Test

In this study, the imaging fluids prepared via different mixing methods were transferred into separate mason jars, as shown in Figure 5-4 below, and their behavior was monitored. It was observed that the temperature of the canola and stearic acid mixture before the addition of barite plays a significant role in the stability of the fluid. The high-temperature mixture before the addition of barite exhibits a more rapid separation of barite over time. This phenomenon is consistent for both types of barites used. However, imaging fluid made with microbarite was observed to be more stable than API barite produced in the same way. The significance of this test is to determine the need for remixing of the imaging fluid when left alone for some time before its use.

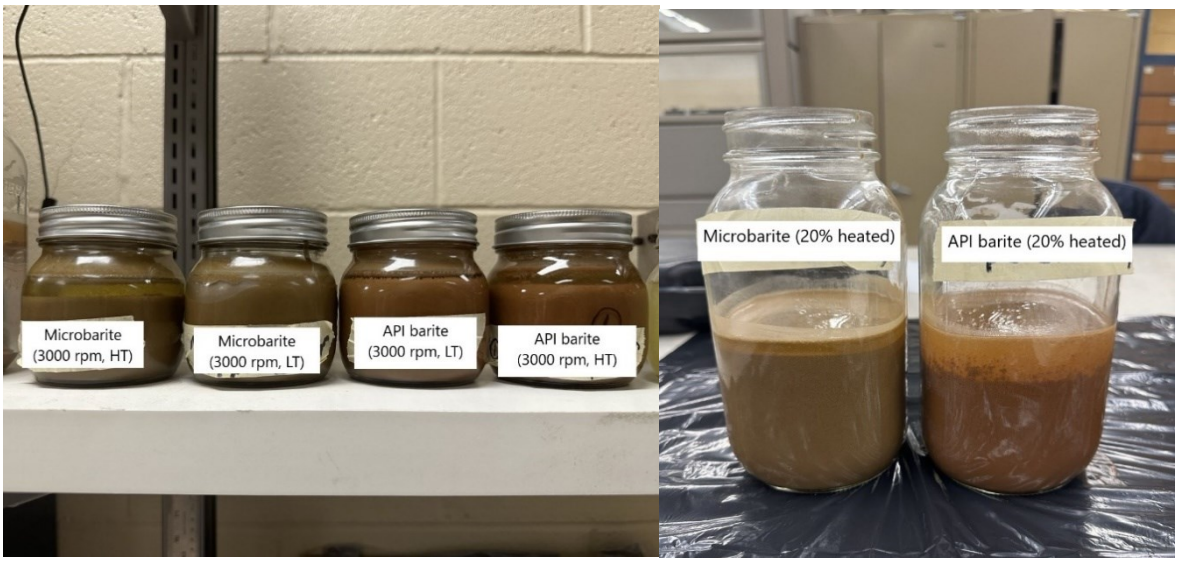

Figure 5-4: Separation test of prepared imaging fluids

5.6.2 Settlement Test

As the prepared imaging fluid reaches room temperature, 100ml of the prepared imaging fluid (each mixing procedure) is poured into 500ml of water with temperatures 5° and 24°c which falls within the range of ground water temperatures experienced downhole. This test is done to check the stability of the imaging fluid in water, as it is desired for the fluid to settle in water. Figures 5-5 to 5-7 show the fluid settlement in water performance. As shown in Table 5-1, imaging fluid produced by agitation at high and low temperatures (both microbarite and API barite) started to separate in water after about an hour to 3 hours with exception to the fluid mixed at 3000rpm and later oven heated that showed good settlement performance alongside that produced with the general protocol method which was seen to show a good settlement performance in water for over 7 days. This can be attributed to the introduction of bubbles because of mixing at high speed for a long period of time, resulting in a lower fluid SG of less than 1.2. Bubbles in the mixture decrease the mass of the fluid over the same fluid volume.

Table 5-1: Settlement in water performance for different mixing procedures and weighting agents

Weighting agent/ Mixing Procedure	Separation time (Hr)	
	In 5 °c water	In 24 °c water
API Barite (3000 rpm, mixed at HT)	1	1
Microbarite (3000 rpm, mixed at HT)	3	3
Microbarite (3000 rpm, mixed at LT)	3	3
API Barite Imaging fluid (3000 rpm + oven heated, mixed at LT)	Good after 7 days	Good after 7 days
API Barite (20% heated)	Good after 7 days	Good after 7 days
Microbarite (20% heated)	Good after 7 days	Good after 7 days

Figure 5-5: Water settlement test for imaging fluid mixed at 3000 rpm and high temperature in 5 and 24°c a) API barite after 1 hr b) after 24 hrs c) Microbarite after 1 hr d) after 24 hrs

Figure 5-6: Water settlement test for imaging fluid mixed at 3000 rpm and low temperature in 5 and 24°c a) API barite (oven-heated) after 1 hr b) after 7 days c) Microbarite after 1 hr d) after 24 hrs

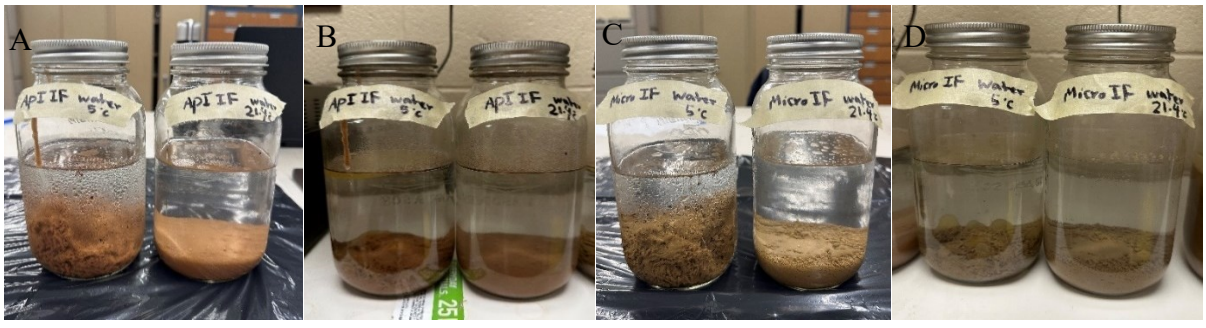

Figure 5-7: Water settlement test for imaging fluid mixed using the general protocol in 5 and 24°c a) API barite after 1 hr b) after 7 days c) Microbarite after 1 hr d) after 7 days

5.6.3 Fluid Rheology Test

In addition to the separation and settlement test, the imaging fluid rheological properties were also measured using the OFFITE 8 speed viscometer and the filter press. Table 5-2 below shows the estimated plastic viscosity, apparent viscosity, yield point and the yield point to plastic viscosity ratio (YP/PV) for all the imaging fluid produced. Figures 5-8 to 5-9 are bar charts illustrating the variation of plastic viscosity, apparent viscosity, yield point, and YP/PV ratio with the different imaging fluid produced. Table 5-3 below shows the estimated flow behavior index, viscosity index, measured density, conductivity, filtrate volume, mud cake thickness obtained from filtration test.

Table 5-2: Imaging fluid plastic viscosity, apparent viscosity, yield point, and YP/PV ratio

Weighting agent/ Mixing Procedure	**Plastic Viscosity (cP)**	**Apparent Viscosity (cP)**	**Yield Point (lb/100ft^2)**	**YP/PV**
API Barite (3000 rpm, mixed at HT)	55	60	10	0.18
Microbarite (3000 rpm, mixed at HT)	66	75	18	0.27
Microbarite (3000 rpm, mixed at LT)	99	121.5	45	0.455
API Barite Imaging fluid (3000 rpm + oven heated, mixed at LT)	84	105	41	0.49
API Barite (20% heated)	59.5	66.3	13.5	0.23
Microbarite (20% heated)	64	68	8	0.13

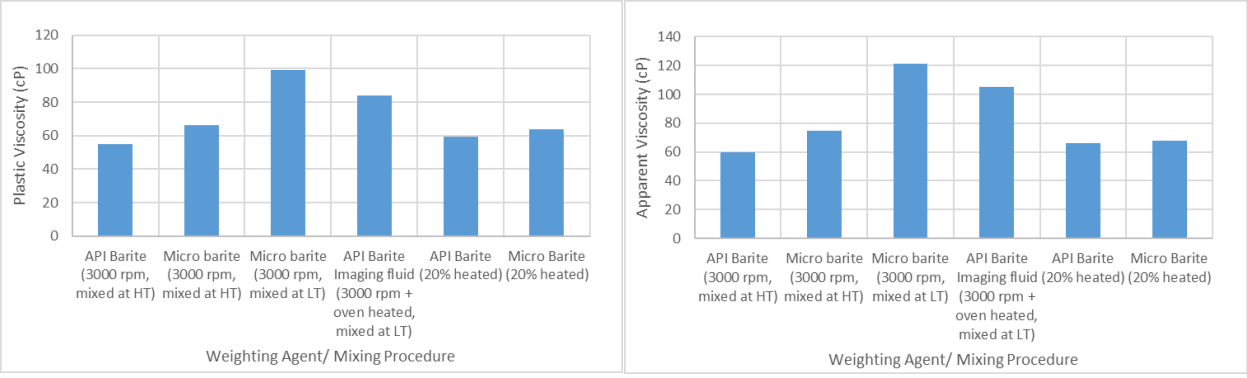

Figure 5-8: Bar charts of imaging fluid plastic and apparent viscosity variations

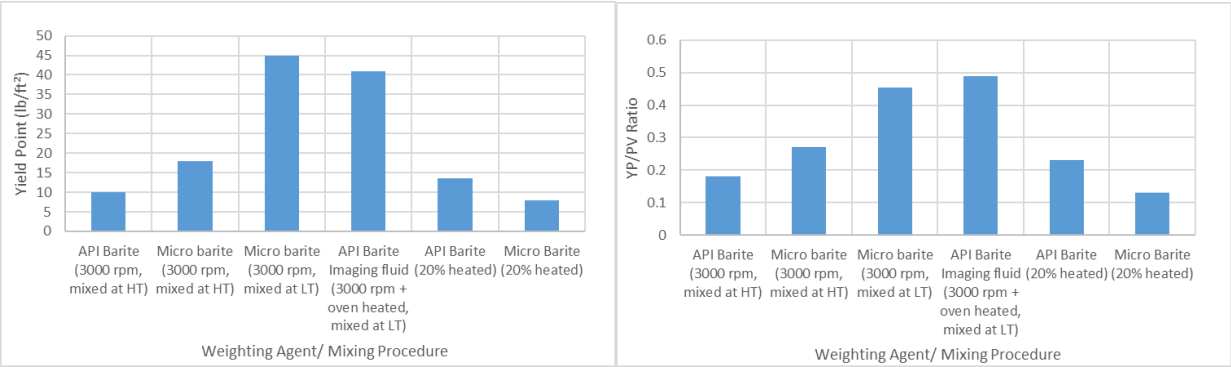

Figure 5-9: Bar charts of imaging fluid yield point and YP/PV ratio variations

Table 5-3: Flow behaviour index, viscosity index, density, conductivity, and filtration test results of prepared imaging fluid

Weighting agent/ Mixing Procedure	**n**	**K**	**Density (g/cc)**	**Filtrate Volume (mL)**	**Mud Cake Thickness (mm)**	**Conductivity (µS/m)**
API Barite (3000 rpm, mixed at HT)	0.884	0.2623	1.19	140	13	0
Microbarite (3000 rpm, mixed at HT)	0.836	0.457	1.07	104	8	0
Microbarite (3000 rpm, mixed at LT)	0.754	1.304	1.05	83	7	0
API Barite Imaging fluid (3000 rpm + oven heated, mixed at LT)	0.741	1.229	1.2	118	10	0
API Barite (20% heated)	0.8595	0.343	1.192	219	21.5	0
Microbarite (20% heated)	0.917	0.2365	1.195	159.5	16.5	0

Figures 5-10 to 5-12 show the pictures of the mud cake formed from the filtration rate test for each imaging fluid produced. In all, microbarite imaging fluid produced in a particular mixing method has a smaller mud cake thickness compared to that produced using API barite.

Figure 5-10: Filtration test mud cake for imaging fluid produced using 3000 rpm mixed at high temperature

Figure 5-11: Filtration test mud cake for imaging fluid produced using 3000 rpm (+ oven heated for API barite) mixed at low temperature

Figure 5-12: Filtration test mud cake for imaging fluid produced using the general protocol

The stability of these imaging fluids (separation test result) can be attributed to their respective yield point values and YP/PV ratios. High yield point and YP/PV ratio signifies greater internal resistance to initial flow, which is advantageous for maintaining fluid stability over time. Therefore, the imaging fluid produced at 3000 rpm, oven heated, and mixed at LT possesses the highest yield point and is the most stable, followed by the Microbarite imaging fluid at LT. These two imaging fluids had a ratio above 0.4. It could be deduced that an imaging fluid of the same quantity (recipe proportion) with a lower ratio would separate very quickly when left with time, which is undesirable.

When comparing imaging fluids made with barite of different particle sizes, it is observed that the fluid containing Microbarite performs better than the one with API barite. Microbarite-based fluid is more desirable due to its lower filtrate volume and thinner mud cake thickness as the filtration rate test indicates. This difference highlights the influence of weighting agent particle size on the properties of the prepared imaging fluid. The flow behavior index (n) of all the imaging fluids prepared is less than 1, confirming the fluids are shear thinning and the higher the viscosity index

(K), the higher the viscosity change rate with temperature change. This temperature-dependent behavior should be considered when selecting or formulating imaging fluids for specific applications.

Based on the measured rheological properties, the most desirable imaging fluid is the Microbarite-based fluid prepared at low temperature, as this imaging fluid has the highest yield point, apparent viscosity, and plastic viscosity. However, from the settlement in water performance tests, this imaging fluid separated after three hours due to introduced bubbles at the mixing step and a lower SG than 1.2, which is the minimum limit for a good performance in water. On the other hand, API barite and Microbarite based imaging fluids made with the original mixing procedure were stable in water even after more than one week (7 days).

5.7 Conclusion & Recommendation

This study has investigated the impact of preparation methods, weighting agent particle size and temperature on the quality of imaging fluid. From the study, agitation can dissolve stearic acid only if the temperature of the mixture is raised by effect of mixing to the melting point of the stearic acid, but it introduces bubbles to the imaging fluid which decreases its specific gravity thereby decreasing its settlement in water performance. Imaging fluids made with Microbarite tend to produce a higher quality fluid compared to Api barite-based imaging fluid.

It is recommended to follow the general protocol in dissolving stearic acid while preparing imaging fluid but mix barite at a low temperature. Future work should focus on developing an imaging fluid recipe that can readily dissolve in a fluid phase without rigorous mixing and heating.

6. Water Based Alternative for Imaging Fluid

This chapter discusses the development of a water-based alternative imaging fluid for Ground Penetrating Radar (GPR) applications. It is a manuscript prepared for publication. This paper is authored by Oluwatimilehin Mary Akindele, Dr. Abdelsalam Abugharara, and Dr. Stephen Butt.

6.1 Abstract

Ground Penetrating Radar (GPR) is a widely used technique for near-surface electromagnetic exploration, reliant on imaging fluids to enhance data quality in the borehole. However, existing oil-based fluids present challenges in terms of cost and logistics. This study proposes a water-based fluid system as an alternative, formulated with tap water, polyoxyethylene sorbitan monolaurate (Tween 20), and barite. Conductivity measurements demonstrated the fluid's ability to reduce electrical conductivity with increasing Tween 20 concentration. GPRMax simulations highlighted the impact of borehole fluid properties on wave propagation, indicating comparable performance between the water-based fluid and oil-based counterparts when dielectric permittivity was set to 3. These findings suggest the potential viability of the water-based fluid for borehole GPR applications, offering environmentally friendly and cost-effective solutions. Further research is needed to validate its performance in real-world conditions and optimize its formulation for specific geological settings.

6.2 Introduction

Ground Penetrating Radar (GPR) is a technique used for borehole electromagnetic exploration, often called echo-sounding. It relies on differences in electromagnetic properties to identify the physical boundaries of shallow structures [77]. Electromagnetic waves are transmitted in the borehole and recorded by the antenna once the waves penetrate into the rock [54]. The media

between the antenna and the wellbore can impact the borehole imaging tool data quality. Groundwater has been proven to influence the data quality of the imaging tool, so it needs to be replaced by an imaging fluid at the bottom hole [78].

The ideal borehole fluid (imaging fluid) should possess certain properties, which include low electrical conductivity, appropriate dielectric permittivity close to that of the host rock, higher density than water to enable it to settle at the bottom hole, and stability such that it does not discompose while imaging. Following the above characteristics, the imaging fluid comprises a fluid base with low dielectric permittivity and conductivity, a weighting agent to increase density over water to about 1.2, and an emulsifier to ensure stability.

This study seeks to propose a water-based fluid system with the appropriate EM properties and the ability to replace groundwater in the borehole during borehole imaging to overcome the challenge around the present oil-based imaging fluid. Some of the challenges faced with the current imaging fluid, which is oil-based, are the cost of production and logistics. This entails the cost of producing the oil-based imaging fluid (procedure explained in detail in Chapter 5) involving a heating process using a heater/ oven. In a real-life scenario, a heater is not readily available at the field and would either be rented or bought and then transported to the field. In cases where the imaging fluid (large scale) is to be produced in the laboratory and transported to the field, logistic issues will be on the high side and not economical.

The key water parameters needed to be optimized to produce a water-based imaging fluid include its Relative Dielectric Permittivity (RDP), conductivity, and magnetic susceptibility.

6.3 Reducing Water Dielectric Permittivity

Dielectric permittivity describes how the displacement of charge within a material structure responds to an electric field, leading to energy storage in the material. High dielectric permittivity indicates a strong response to the electric field, while low permittivity suggests a weaker response [81]. Groundwater has a relatively high dielectric permittivity, and can easily undergo charge displacement when subjected to an electric field. This property is significant in various scientific and technological applications, such as electromagnetic exploration.

The relative dielectric permittivity of groundwater, approximately 80, can be reduced by incorporating substances with a lower dielectric constant [82]. Such materials include acrylic rods [83], nickel hydroxide [84], polyvinyl chloride [85], polyethylene powder [86-89], polyoxyethylene sorbitan monolaurate [90,91], ethylene glycol [91,92], and sugar (sucrose) [82, 93-95]. The permittivity decreases linearly with increasing any of the above materials.

In this study, polyoxyethylene sorbitan monolaurate, also known as Tween 20, is explored to reduce the dielectric permittivity of water and produce a new potential imaging fluid (water-based). Research done by Fukunaga et al. in 2005 [90] to investigate the dielectric properties of tissue-equivalent liquids for radio wave safety tests involved a recipe of Tween 20 in deionized water. They were able to achieve a mixture of the required permittivity of less than 10 easily with Tween 20 as seen in Figure 6-1 below.

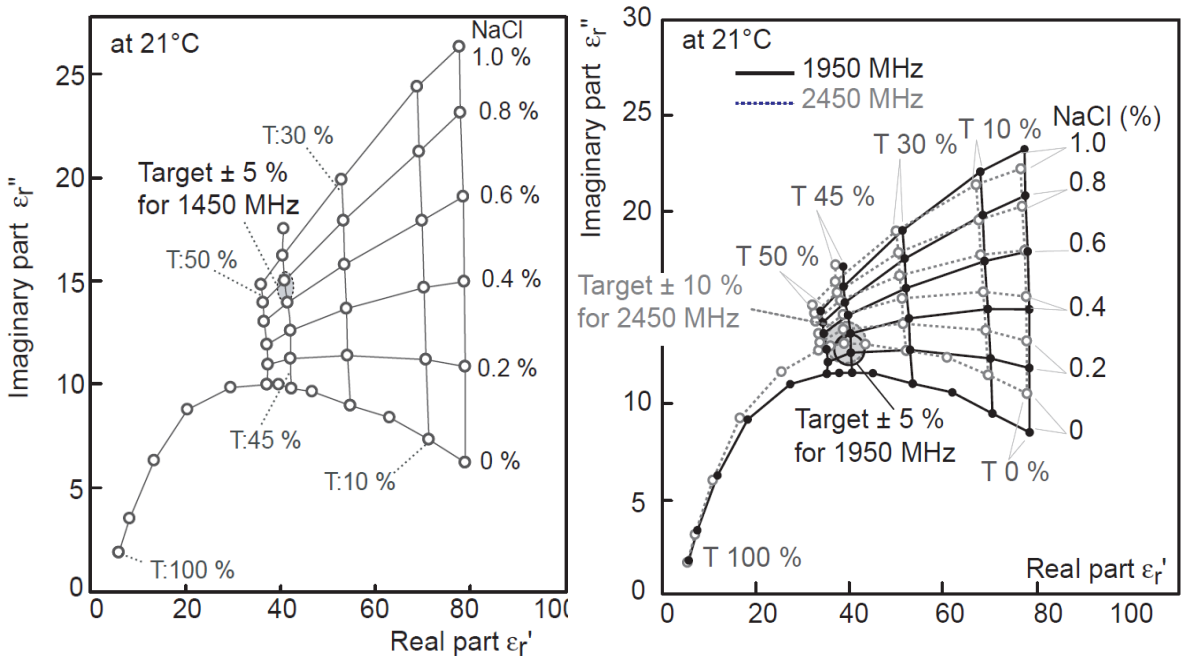

Figure 6-1: Permittivity matrix for fluid mixture with Tween 20 from Fukunaga et al. research [90]

Polyoxyethylene sorbitan monolaurate is stable, nontoxic, and biodegradable with low irritation potential [91] and doubles as an emulsifier. It is a non-ionic surfactant widely used as an emulsifier and stabilizer in the pharmaceutical, food, paint, and cosmetic industries [96,97].

6.4 Material and Methods

The new imaging fluid recipe involves materials such as:

- Fluid base: Fresh (tap) water with a dielectric constant of 80
- Additive/ Emulsifier: Polyoxyethylene sorbitan monolaurate (Tween 20), which helps to reduce water dielectric permittivity and also serve as an emulsifier.
- Weighting agent: Barite to increase the density of the mixture to 1.2g/cc, allowing for the settlement of the imaging fluid downhole.

6.4.1 Conductivity Measurement

Aside from the fluid dielectric permittivity, conductivity is another important parameter of imaging fluid, as GPR thrives in low electrical loss materials. In this research, the conductivity of water

and Tween 20 mixture is first examined using a conductivity meter to check the effect of Tween 20 on water conductivity. Here, 500ml of water is measured in a glass jar, and the conductivity of water and Tween 20 is first measured separately. Tween 20 is then added to the water in stages with an initial volume concentration of 25% (125ml) and an increment of 25%, resulting in 50%, 75%, and 100% concentration levels, respectively. The fluid mixture's temperature and conductivity are measured and recorded at each concentration level. This test was done using both deionized water and tap water. Figure 6-2 is a picture of the conductivity meter used for the conductivity measurement. It has the capability to measure the conductivity and temperature of the mixture.

Figure 6-2: Conductivity meter used for the experiment

6.4.2 GPR Simulation

This step involves simulating a 2D GPR model considering four different borehole fluids, which include free space (air), water, Oil-based Imaging fluid described in Chapter 5, and the alternative imaging fluid proposed (water-based) to compare responses and their effect on the field signal and

strength. From previous research, experiments, and further buttressed by the GPR simulation, an air-filled borehole has been seen to allow GPR signals penetrate to a great depth due to its electrical properties. The major aim of this simulation process is to see the effect of water and Tween 20 conductivity, assuming we have the required dielectric permittivity for the mixture on the GPR model. This simulation is done using GPRMax. GPRMax is an open-source software that simulates the transmission of electromagnetic waves employing the Finite Difference Time Domain (FDTD) technique for numerically modelling GPR and the output from the software is represented using A-Scan and B-Scan signal [54, 55].

Based on the result of the conductivity test, magnetic properties, and already published data for dielectric permittivity of fluid in Fukunaga et al research [90], GPRMax 2D modeling was performed using air, water, oil-based imaging fluid, and the proposed water-based imaging fluid as the simulation borehole fluid. The borehole fluid properties used for the simulation are presented in Table 6-1 below. The rock property used in the simulation is a conductivity of 0, a dielectric permittivity of 4, a magnetic permeability of 1, and a magnetic loss of 0.

Table 6-1: Borehole fluid properties used for GPRMax 2D simulation

Borehole Fluid	Conductivity (S/m)	Dielectric Permittivity	Magnetic Permeability	Magnetic Loss
Air	0	1	1	0
Tap Water	0.1	80	1	0
Oil-based imaging fluid	0	3	1	0
Water-based imaging fluid	0.023	3/ 10	1	0

6.4.3 GPRMax Design and Simulation

Figure 6-3 highlights some of the commands used for GPRMax 2D simulation and their function. The command and specifications used in designing this research simulation were the domain size,

spatial step, borehole size, rock size, transmitter/ receiver position, and time window shown in Table 6-2 below.

Command	Function
#domain:	Controls the physical size of the model
#dx_dy:	Defines the discretization steps
#time_window:	Defines the simulated time window for the GPR trace
#medium:	Introduces the electrical properties of different media in the model
#box:	Introduce a rectangle of specific properties into the models space
#cylinder:	Like the box: but introduces a cylinder into the model
#triangle:	Like the box: but introduces a triangular patch.
#tx:	Specifies the details of a transmitter (Tx)
#rx:	Specifies the details of a receiver (Rx)
#scan:	Can be used to automatically generate B-Scans

Figure 6-3: A Table showing some GPRMax 2D commands [56]

Table 6-2: GPRMax design specification

Function	Command	Specification
Domain (physical size of the model in meters)	#domain:	5 5 0.002
Discretization step (should be at least ten times smaller than the shortest wavelength of the propagating electromagnetic field)	#dx_dy_dz:	0.002 0.002 0.002
Borehole (Mat X) size (1 by 5 meters)	#box:	0 0 0 1 5 0.002 matX
Rock (Mat Y) size (4 by 5meters)	#box:	1 0 0 5 5 0.002 matY
Time window (secs)	#time_window:	10e-9
GPR antenna	#waveform:	1.5GHz my_ricker
Transmitter position (0.5 by 2.5 meters)	#hertzian_dipole	0.5 2.5 0 my_ricker
Receiver position (0.54 by 2.5 meters)	#rx	0.54 2.5 0

6.5 Result and Discussion

6.5.1 Conductivity Test Result

Conductivity measurements were performed to determine water (deionized and Tap) and Tween 20 Conductivity. The result of the conductivity measurement is shown in Table 6-3.

Table 6-3: Conductivity measurement result

Volume (ml) Deionize water	Volume (ml) Tap water	Volume (ml) Tween 20	Temperature (°c)	Conductivity (µS/cm)
500	-	-	17.4	1.98
-	500	-	23.8	164.4
-	-	125	19.2	0.53
500	-	125	23.3	160.7
500	-	250	26	134.3
500	-	375	28.4	64.3
500	-	500	28	114.4
-	500	125	27.2	225.3
-	500	250	31.6	96.5
-	500	375	32.5	74.8
-	500	500	32.1	105.9

The same trend of conductivity result was observed for both deionized water and tap water when mixed with Tween 20. Tap water, when mixed with 25% Tween concentration, raises the conductivity of the mixture to 225.3 µS/cm. There is a decrease in conductivity with an increase in temperature up to 75% concentration level of Tween 20. The conductivity then increased again at 100% Tween concentration. For the simulation, the highest conductivity value was used which is the value at 25% Tween 20 concentration value with Tap water. Figure 6-4 shows the graph of the conductivity trend of Tween 20 at different concentration with water (deionized and tap).

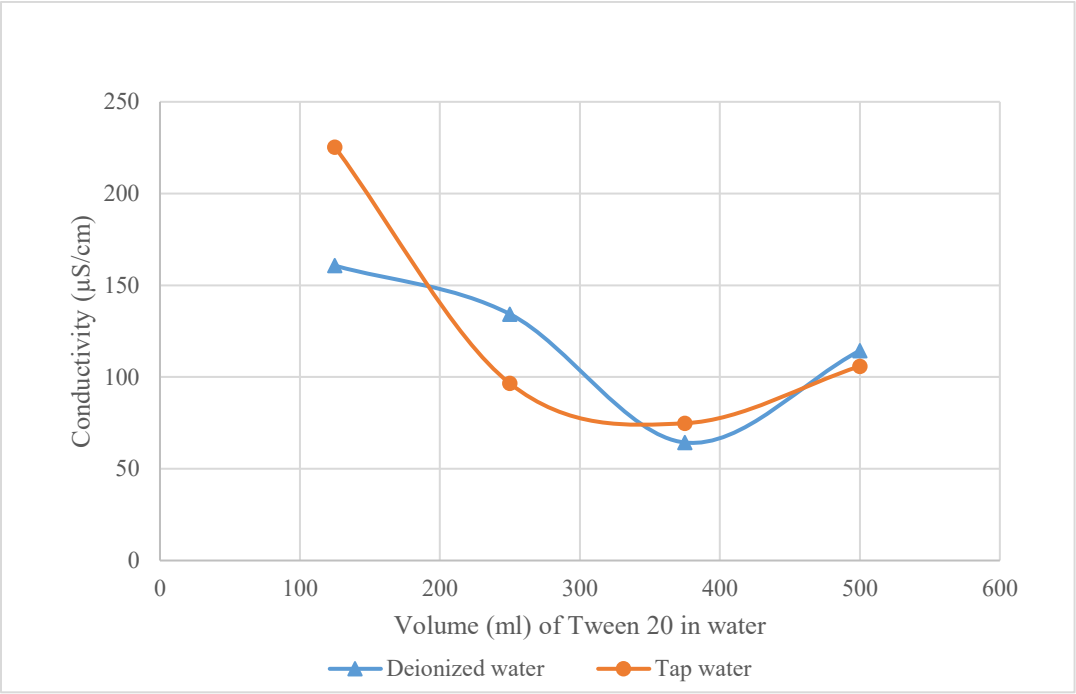

Figure 6-4: Graph showing the conductivity of Water + Tween 20 at different Tween 20 concentration level using both Deionized Water and Tap Water

6.5.2 GPR Simulation Result

The geometry of the problem simulated consists of a 1m by 5m borehole size and a 4m by 5m rock size. Figure 6-5 below is the pictorial view of the geometry simulated where the blue legend represents the borehole and red represents the rock sample.

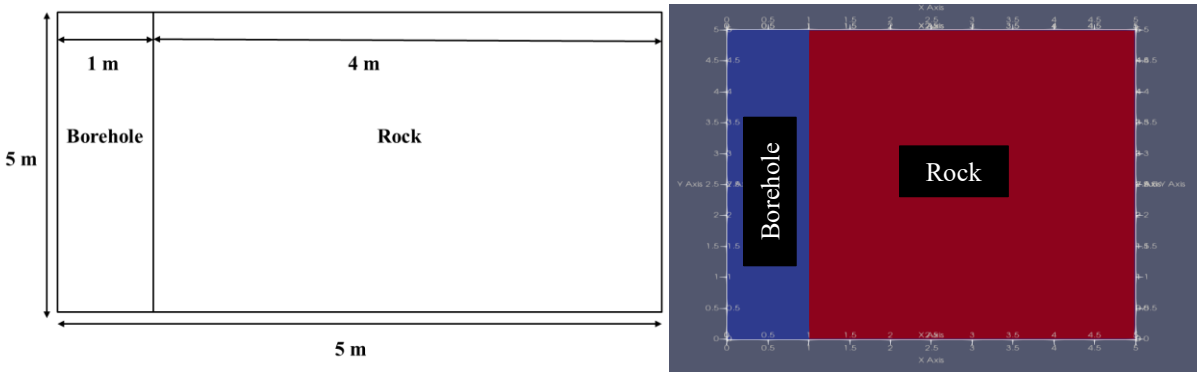

Figure 6-5: GPRMax 2D simulated geometry

A

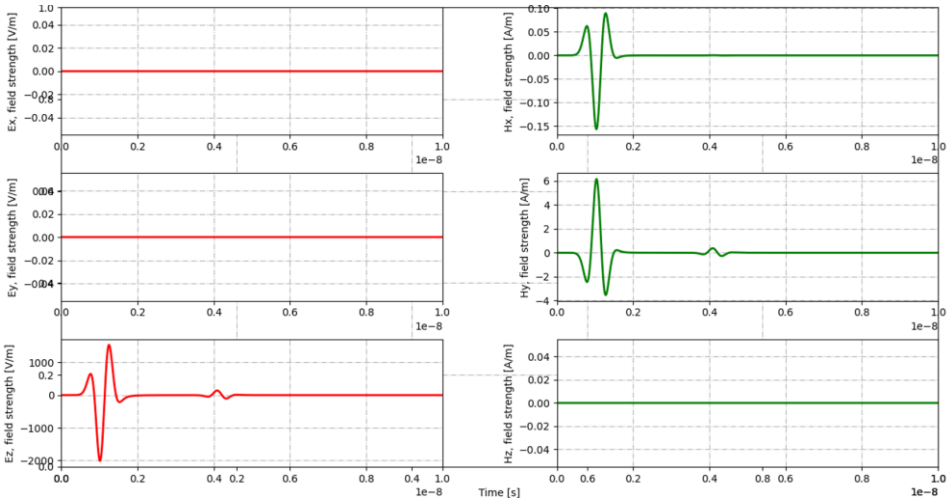
Ex, field strength [V/m]
Ey, field strength [V/m]
Ez, field strength [V/m]
Hx, field strength [A/m]
Hy, field strength [A/m]
Hz, field strength [A/m]
Time [s]
1e−8

B

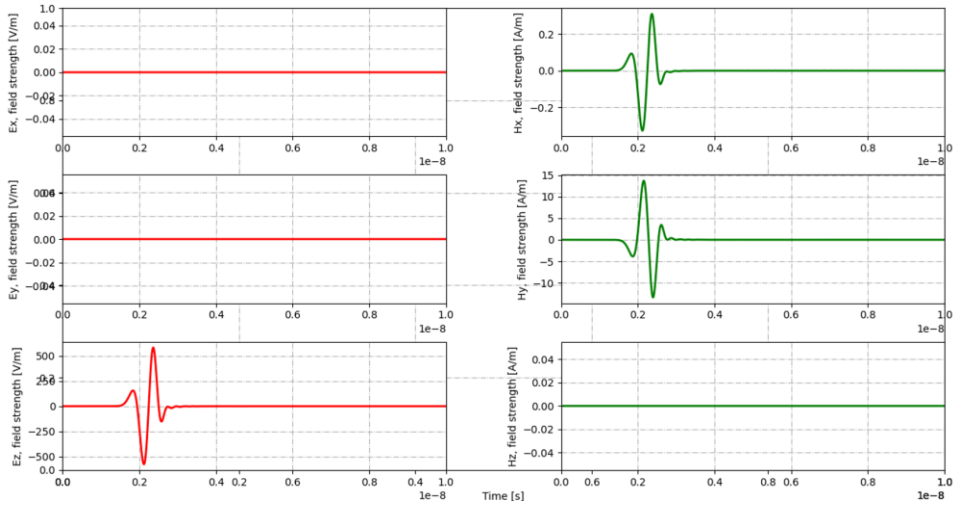
Ex, field strength [V/m]
Ey, field strength [V/m]
Ez, field strength [V/m]
Hx, field strength [A/m]
Hy, field strength [A/m]
Hz, field strength [A/m]
Time [s]
1e−8

C

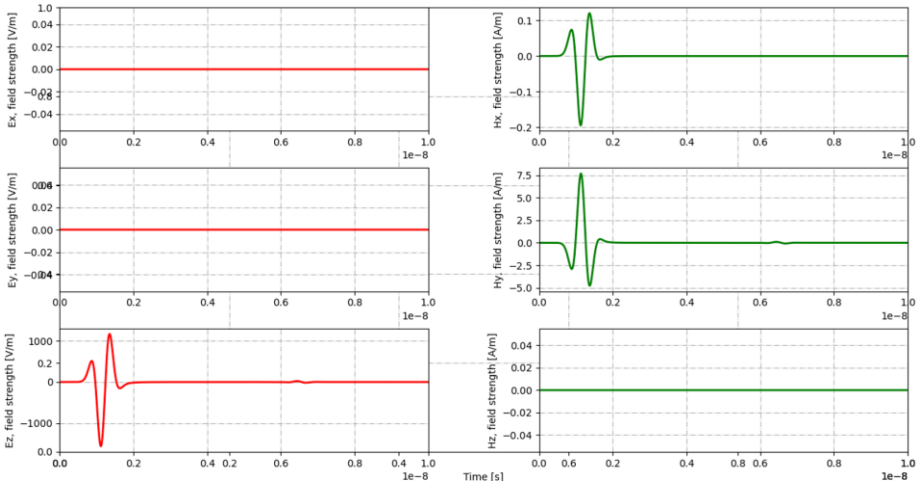
Ex, field strength [V/m]
Ey, field strength [V/m]
Ez, field strength [V/m]
Hx, field strength [A/m]
Hy, field strength [A/m]
Hz, field strength [A/m]
Time [s]
1e−8

D

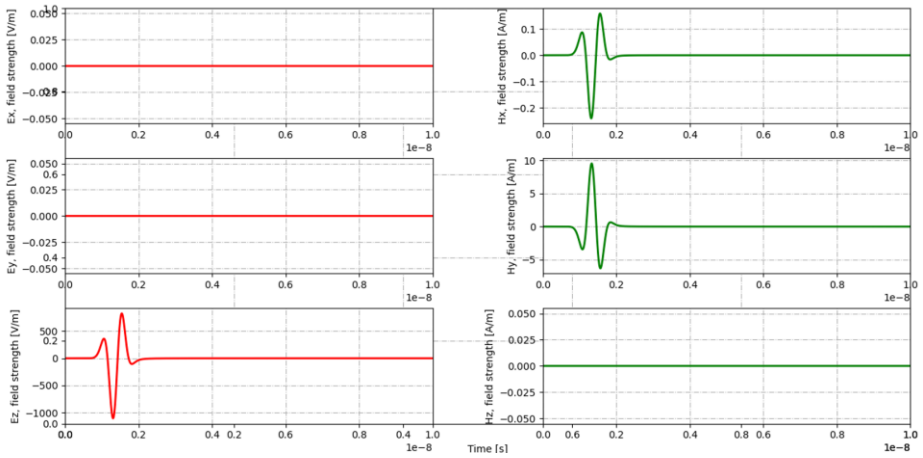

E

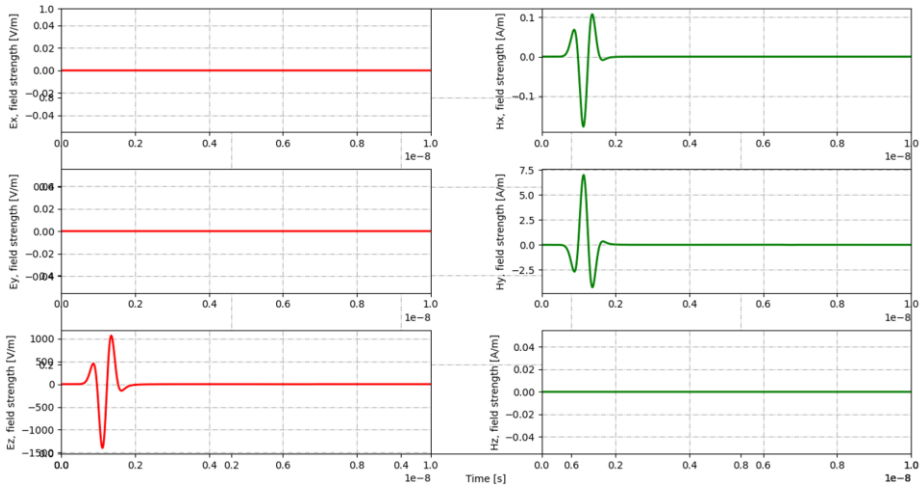

Figure 6-6:A-Scans of wave propagation into the rock with different borehole fluids (A) Air-filled borehole (B) Water-filled borehole (C) Oil-based imaging fluid-filled borehole (D) Water-based imaging fluid-filled borehole at RDP of 10 (E) Water-based imaging fluid filled borehole at RDP of 3

Table 6-4: Peak amplitude/ Field strength of signals based on the borehole fluid

Borehole Fluid	**Peak Amplitude/ Field Strength (V/m)**
Air	1570
Tap Water	593
Oil-based imaging fluid	1190
Water-based imaging fluid (RDP=10)	860
Water-based imaging fluid (RDP=3)	1090

Figure 6-6 shows the A-scan obtained from the simulation. It represents the model time history of the electric and magnetic field components and currents at the receiver. It is the amplitude of the reflected waves as a function of time. From the A-scans, the impact of the borehole fluid can be

seen on the strength and timing of the reflected signals. An air-filled borehole is seen to have the highest amplitude of 1570 V/m, followed by the oil-based imaging fluid-filled borehole with 1190 V/m, then water-based imaging fluid-filled borehole when an RDP of 3 is achieved with an amplitude of 1090 V/m. The water-based imaging fluid-filled borehole at RDP of 10 has an amplitude of 860 V/m, while water-filled imaging fluid has the least amplitude of 593 V/m.

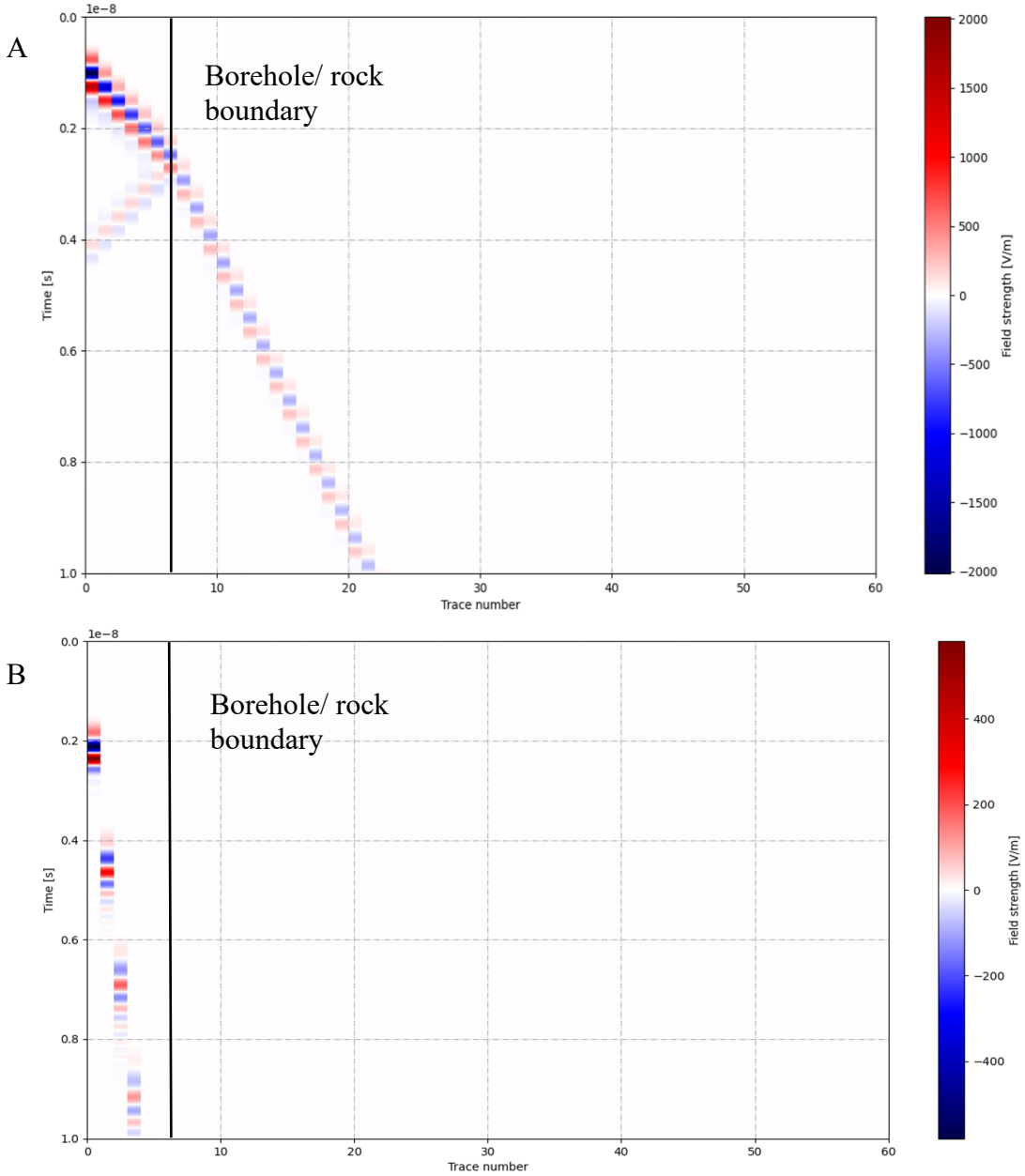

C

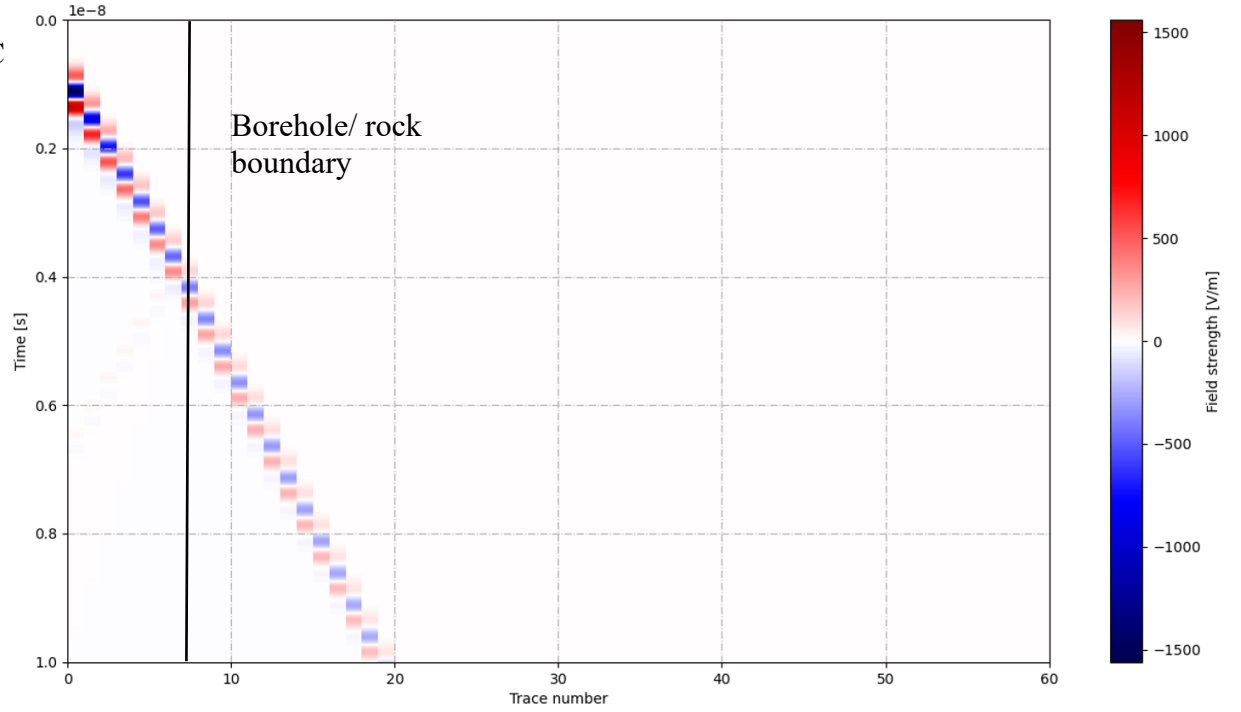
1e−8
Borehole/ rock boundary
Time [s]
Trace number
Field strength [V/m]

D

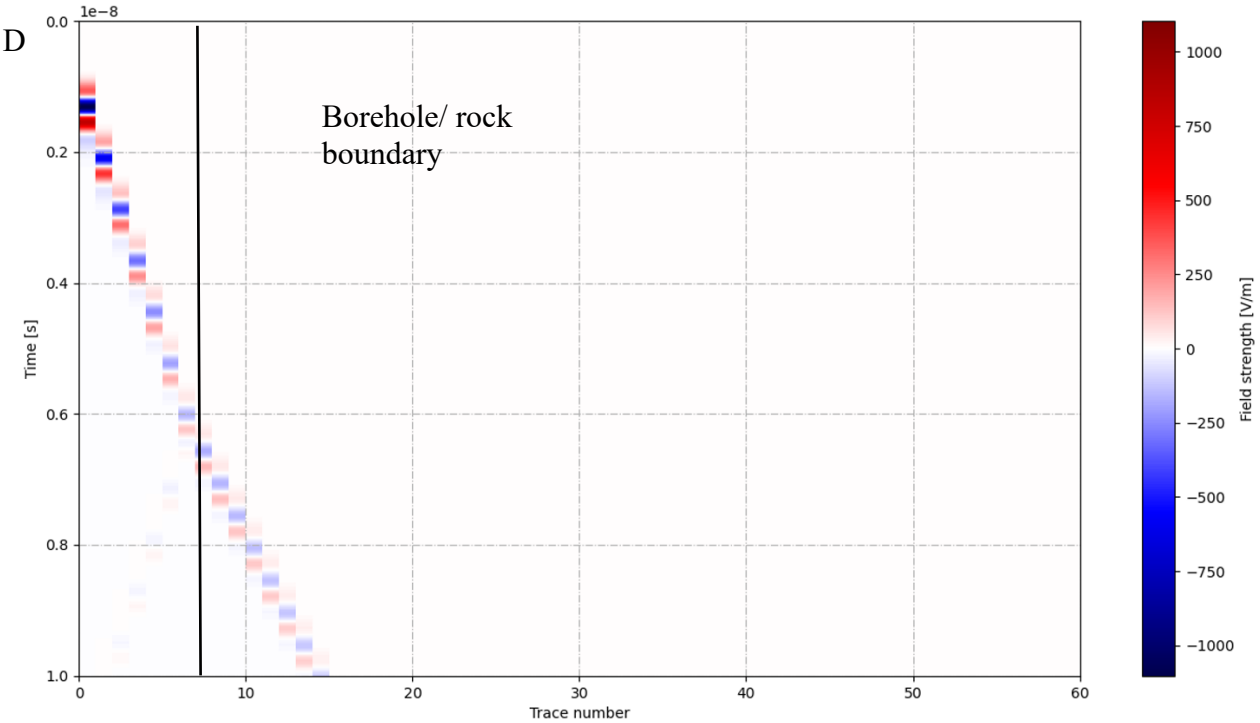
1e−8
Borehole/ rock boundary
Time [s]
Trace number
Field strength [V/m]

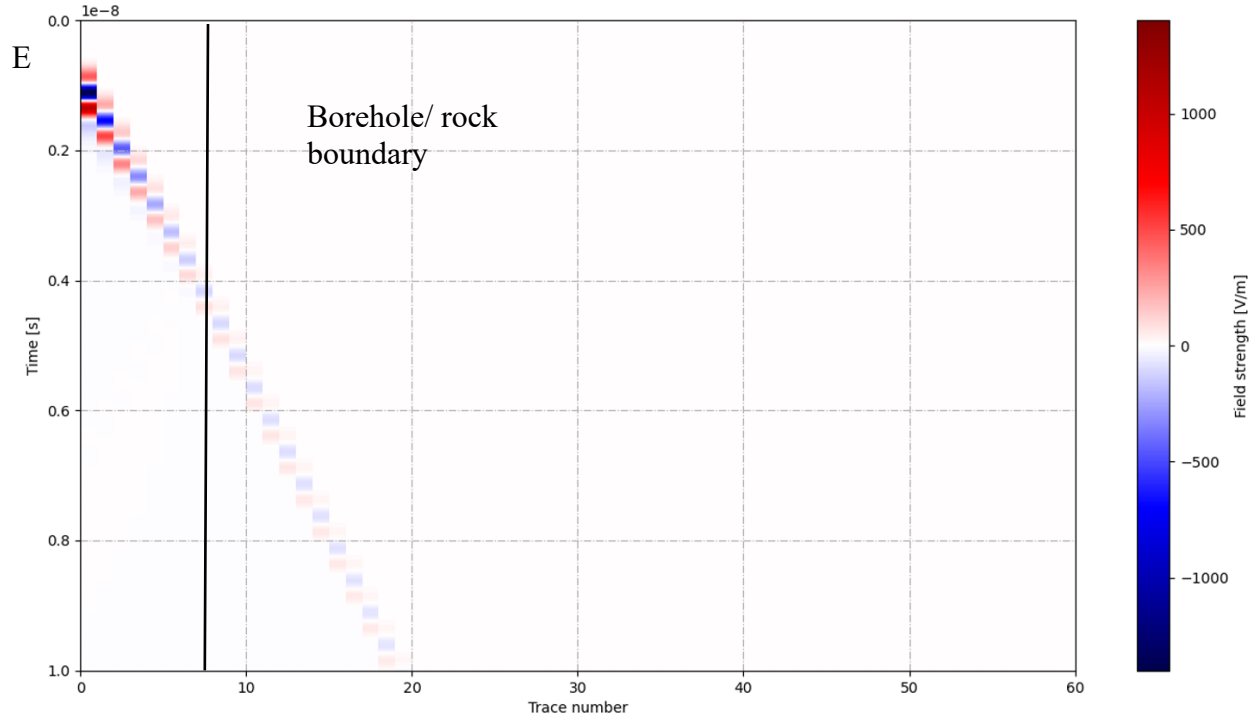

Figure 6-7: B-Scans of wave propagation into the rock with different borehole fluids (A) Air-filled borehole (B) Water-filled borehole (C) Oil-based imaging fluid-filled borehole (D) Water-based imaging fluid-filled borehole at RDP of 10 (E) Water-based imaging fluid filled borehole at RDP of 3

Figures 6-7 illustrate the B-Scans of wave propagation into the rock with different borehole fluid using a 1.5GHz antenna model. A B-scan is composed of multiple traces (A-scan) recorded as the receiver is moved from the borehole into the rock. In this model, the receivers are placed at different distances from the source with incremental grid spacing of 7.5 cm for 60 runs. As expected, an increase in the dielectric constant resulted in a decrease in the velocity and wavelength. Air with the lowest dielectric constant had an increased depth of signal penetration and water with the lowest signal penetration depth showing the impact of fluid dielectric constant on GPR. When the dielectric constant of the water-based imaging fluid was set to 3, it had a signal penetration depth close to that of the oil-based imaging fluid compared to when it was set to 10.

This implies that the dielectric permittivity of the fluid has a much greater effect on wave propagation using GPR than the conductivity of the water-based imaging fluid.

At about a trace number of 7, which is the boundary between the borehole and the rock, signal reflection is observed when the borehole is filled with air. There is also a reduction in the wave velocity attributed to the difference in dielectric constant of air and rock with air having the lowest RDP. For water filled borehole, the signal didn't penetrate the rock as a result of its high dielectric constant while for oil-based imaging fluid-filled borehole and water-based imaging fluid-filled borehole at RDP of 3, there is no change in the wave velocity. This is because the closeness of the dielectric constant of both rock and the fluid which is not the same with the water-based imaging fluid filled borehole at RDP of 10. There is an increase in the wave velocity into rock compared to the borehole when the water based imaging fluid at RDP of 10 is the borehole fluid, hence the change in the signal slope but with a reduced signal penetration depth. This study shows how energy partitions when the EM wave encounters a contrast in properties.

6.6 Conclusion and Recommendation

In conclusion, this study proposes a water-based imaging fluid system as a promising alternative to oil-based imaging fluids for Ground Penetrating Radar (GPR) applications, aiming to address the challenges of cost and logistics associated with the current oil-based option. Formulated with tap water as the base fluid, polyoxyethylene sorbitan monolaurate (Tween 20) as a dielectric permittivity reducer and emulsifier, and barite as a weighting agent, the proposed fluid meets specific criteria including low electrical conductivity, appropriate dielectric permittivity matching that of the host rock, increased density for settling, and stability during imaging. GPRMax simulations revealed the impact of borehole fluid properties on wave propagation, with variations in dielectric permittivity significantly affecting signal strength, penetration depth and timing.

Particularly when the dielectric permittivity was set to 3, the water-based imaging fluid showed comparable performance to the oil-based counterpart irrespective of the conductivity value, suggesting its potential viability in borehole GPR applications. Further research and field testing is needed to confirm the feasibility of attaining dielectric permittivity of 3 for the water-based imaging fluid, validate its performance under real-world conditions, and optimize its formulation for specific geological settings, offering promising insights into environmentally friendly and cost-effective solutions for borehole imaging technology.

7. Conclusion and Recommendation

In conclusion, this broad exploration into large diameter drilling represents a significant contribution to the field, unraveling intricate facets that play pivotal roles in optimizing rock excavation performance. The multifaceted approach, spanning borehole imaging, imaging fluid properties and development of a water-based imaging fluid, cuttings cleaning efficiency, 3D scanning for volume estimation, collectively advances our understanding of large diameter drilling operations.

- Cuttings cleaning efficiency emerges as a critical factor influencing disc cutter drilling performance. The experiments conducted employing different evacuation methods, underscore the tangible impact of cleaning efficiency on drilling operations. These findings have direct implications for improving overall efficiency, speed, and cost-effectiveness in large diameter drilling.
- The innovative use of a 3D scanner for estimating rock excavated volume brings a new dimension to drilling performance assessment. By offering precise measurements of rock chip volume, this method provides valuable data for calculating specific energy and, consequently, optimizing drilling operations. Future work will involve exploration into alternative scanning methods for illuminated rock surfaces.
- The exploration of imaging fluid rheological properties, considering factors like agitation and temperature, adds depth to our knowledge. The comparison of different fluid preparation methods and weighting agent grain sizes unveils nuances in stability and settling properties under diverse conditions, offering practical insights for fluid optimization.
- Finally, the study explores the development of a water-based imaging fluid for borehole imaging technology, addressing challenges associated with cost and logistics of existing oil-

based fluids. Through conductivity measurements and GPR simulations, the proposed fluid demonstrates potential as a sustainable solution for borehole GPR applications, offering comparable performance to oil-based imaging fluid while emphasizing environmental friendliness and cost effectiveness. Future work will involve fluid dielectric permittivity testing to confirm the possibility of an RDP of 3 for the water-based imaging fluid and validate its performance under real-world conditions.

Collectively, this thesis endeavors to enhance the planning, design, and execution of large diameter drilling projects across varied geological formations. By addressing these intricate aspects, the research contributes to the overarching goal of achieving precision, efficiency, and cost-effectiveness in large diameter drilling operations. The findings presented herein provide a robust foundation for future research endeavors and practical applications in the dynamic and challenging field of large diameter drilling.

Reference(s)

[1] Cho, J. W., Jeon, S., Jeong, H. Y., & Chang, S. H. (2013). Evaluation of cutting efficiency during TBM disc cutter excavation within a Korean granitic rock using linear-cutting-machine testing and photogrammetric measurement. *Tunnelling and Underground Space Technology*, *35*, 37-54.

[2] Adewale, F. J., Lucky, A. P., Oluwabunmi, A. P., & Boluwaji, E. F. (2017). Selecting the most appropriate model for rheological characterization of synthetic based drilling mud. *Int. J. Appl. Eng. Res*, *12*(18), 7614-7629.

[3] Agrawal, A. K., Chattopadhyaya, S., & Murthy, V. M. S. R. (2021). Delineation of cutter force and cutter wear in different edge configurations of disc cutters–An analysis using discrete element method. *Engineering Failure Analysis*, *129*, 105727.

[4] Zhang, Q., Zhu, Y., Du, C., Du, S., Shao, K., & Jin, Z. (2022). Dynamic rock-breaking process of TBM disc cutters and response mechanism of rock mass based on discrete element. *Advances in Civil Engineering*, *2022*, 1-10.

[5] Labra, C., Rojek, J., & Onate, E. (2017). Discrete/finite element modelling of rock cutting with a TBM disc cutter. *Rock Mechanics and Rock Engineering*, *50*, 621-638.

[6] Yagiz, S., Rostami, J., Kim, T., Ozdemir, L., & Merguerian, C. (2009, October). Factors influencing performance of hard rock tunnel boring machines. In *ISRM EUROCK* (pp. ISRM-EUROCK). ISRM.

[7] Li, B., Zhang, B., Hu, M., Liu, B., Cao, W., & Xu, B. (2022). Full-scale linear cutting tests to study the influence of pre-groove depth on rock-cutting performance by TBM disc cutter. *Tunnelling and Underground Space Technology*, *122*, 104366.

[8] Cho, J. W., Jeon, S., Yu, S. H., & Chang, S. H. (2010). Optimum spacing of TBM disc cutters: A numerical simulation using the three-dimensional dynamic fracturing method. *Tunnelling and Underground Space Technology*, *25*(3), 230-244.

[9] Xia, Y. M., Guo, B., Cong, G. Q., Zhang, X. H., & Zeng, G. Y. (2017). Numerical simulation of rock fragmentation induced by a single TBM disc cutter close to a side free surface. *International Journal of Rock Mechanics and Mining Sciences*, *91*, 40-48.

[10] Xu, H., Geng, Q., Sun, Z., & Qi, Z. (2021). Full-scale granite cutting experiments using tunnel boring machine disc cutters at different free-face conditions. *Tunnelling and Underground Space Technology*, *108*, 103719.

[11] Zhang, Z., Zhang, K., Dong, W., & Zhang, B. (2020). Study of rock-cutting process by disc cutters in mixed ground based on three-dimensional particle flow model. *Rock Mechanics and Rock Engineering*, *53*, 3485-3506.

[12] Balci, C., & Bilgin, N. (2007). Correlative study of linear small and full-scale rock cutting tests to select mechanized excavation machines. *International Journal of Rock Mechanics and Mining Sciences*, *44*(3), 468-476.

[13] Rostami, J. (1997). *Development of a force estimation model for rock fragmentation with disc cutters through theoretical modeling and physical measurement of crushed zone pressure* (Vol. 38, pp. 56-64). Golden, CO, USA: Colorado School of Mines.

[14] Bilgin, N. (1977). *Investigations into the mechanical cutting characteristics of some medium and high strength rocks* (Doctoral dissertation, Newcastle University).

[15] Chang, S. H., Choi, S. W., Bae, G. J., & Jeon, S. (2006). Performance prediction of TBM disc cutting on granitic rock by the linear cutting test. *Tunnelling and Underground Space Technology*, *21*(3), 271.

[16] Qi, G., Zhengying, W., Hao, M., & Qiao, C. (2016). Numerical and experimental research on the rock-breaking process of tunnel boring machine normal disc cutters. *Journal of Mechanical Science and Technology*, *30*, 1733-1745.

[17] Zhang, M. Q., Gou, B., Mo, J. L., Duan, W. J., & Zhou, Z. R. (2022). Rock-cutting and wear performance of a novel TBM disc cutter with spiral grooves. *Tunnelling and Underground Space Technology*, *129*, 104660.

[18] Snowdon, R. A., Ryley, M. D., & Temporal, J. (1982, June). A study of disc cutting in selected British rocks. In *International Journal of Rock Mechanics and Mining Sciences & Geomechanics Abstracts* (Vol. 19, No. 3, pp. 107-121). Pergamon.

[19] Gertsch, R., Gertsch, L., & Rostami, J. (2007). Disc cutting tests in Colorado Red Granite: Implications for TBM performance prediction. *International Journal of rock mechanics and mining sciences*, *44*(2), 238-246.

[20] Zhang, K., Liu, W., Yao, X., Peng, C., Liu, J., & Zheng, X. (2022). Investigation on two-step simulation modeling method for rock breaking by TBM disc cutters assisted with laser. *KSCE Journal of Civil Engineering*, *26*(6), 2966-2978.

[21] Wang, F., Zhou, D., Zhou, X., Xiao, N., & Guo, C. (2020). Rock breaking performance of TBM disc cutter assisted by high-pressure water jet. *Applied Sciences*, *10*(18), 6294.

[22] Balci, C.*, Demircin, MA**, Copur, H.* & Tuncdemir, H. (2004). Estimation of optimum specific energy based on rock properties for assessment of roadheader performance (567BK). *Journal of the Southern African Institute of Mining and Metallurgy*, *104*(11), 633-641.

[23] Wang, X., Su, O., & Wang, Q. F. (2022). Distribution characteristics of rock chips under relieved and unrelieved cutting conditions. *International Journal of Rock Mechanics and Mining Sciences*, *151*, 105048.

[24] Huang, D., Wang, X., Su, O., Zheng, Z. J., & Gao, M. (2022). Study on the cuttability characteristics of granites under conical picks by indentation tests. *Bulletin of Engineering Geology and the Environment*, *81*(5), 192.

[25] Che, D., Zhang, W., Zhu, Z., & Ehmann, K. F. (2018). Rock fails in shearing as a tuned critical system. *International Journal of Rock Mechanics and Mining Sciences*, *110*, 133-139.

[26] Liu, K., Li, X. P., & Liang, S. Y. (2007). The mechanism of ductile chip formation in cutting of brittle materials. *The International Journal of Advanced Manufacturing Technology*, *33*, 875-884.

[27] Nishimatsu, Y. (1972, March). The mechanics of rock cutting. In *International Journal of Rock Mechanics and Mining Sciences & Geomechanics Abstracts* (Vol. 9, No. 2, pp. 261-270). Pergamon.

[28] Loui, J. P., & Rao Karanam, U. M. (2012). Numerical studies on chip formation in drag-pick cutting of rocks. *Geotechnical and Geological Engineering*, *30*, 145-161.

[29] Rostami, J. (1997). *Development of a force estimation model for rock fragmentation with disc cutters through theoretical modeling and physical measurement of crushed zone pressure* (Vol. 38, pp. 56-64). Golden, CO, USA: Colorado School of Mines.

[30] Rad, P. F., & Olson, R. C. (1974). *Tunneling Machine Research: Interaction Between Disk-cutter Grooves in Rocks* (Vol. 7881). US Department of the Interior, Bureau of Mines.

[31] Altindag, R. (2010). Assessment of some brittleness indexes in rock-drilling efficiency. *Rock mechanics and rock engineering*, *43*, 361-370.

[32] Kolapo, P. (2021). Investigating the effects of mechanical properties of rocks on specific energy and penetration rate of borehole drilling. *Geotechnical and Geological Engineering*, *39*(2), 1715-1726.

[33] Duan, Y., Yuan, D., Wu, J., Deng, X., Wu, B., & Sun, Z. (2022). Effect of the Geometric Configuration of the Disc Cutter on the Cutting Behaviour in Tunneling. *Applied Sciences*, *13*(1), 72.

[34] Huo, J., Sun, W., Chen, J., & Zhang, X. (2011). Disc cutters plane layout design of the full-face rock tunnel boring machine (TBM) based on different layout patterns. *Computers & industrial engineering*, *61*(4), 1209-1225.

[35] Xia, Y., Zhang, K., & Liu, J. (2015). Design optimization of TBM disc cutters for different geological conditions. *World Journal of Engineering and Technology*, *3*(04), 218.

[36] Dagrain, F., Detournay, E., & Richard, T. (2001). Influence of the cutter geometry in rock cutting: an experimental approach. *University of Minnesota, Minneapolis*.

[37] Bilgesu, I., Sunal, O., Tulu, I. B., & Heasley, K. A. (2008, June). Modeling rock and drill cutter behavior. In *ARMA US Rock Mechanics/Geomechanics Symposium* (pp. ARMA-08). ARMA.

[38] Gou, B., & Zhang, M. (2022). Effects of surface grooves on rock cutting performance and contact behavior of a TBM disc cutter. *Engineering Fracture Mechanics*, *267*, 108466.

[39] Roxborough, F. F., & Phillips, H. R. (1975, December). Rock excavation by disc cutter. In *International journal of rock mechanics and mining sciences & geomechanics abstracts* (Vol. 12, No. 12, pp. 361-366). Pergamon.

[40] Wang, T., Yan, C., Zheng, H., Ke, W., & Ali, S. (2023). Optimum spacing and rock breaking efficiency of TBM double disc cutters penetrating in water-soaked mudstone with FDEM. *Tunnelling and Underground Space Technology*, *138*, 105174.

[41] Gertsch, R., Gertsch, L., & Rostami, J. (2007). Disc cutting tests in Colorado Red Granite: Implications for TBM performance prediction. *International Journal of rock mechanics and mining sciences*, *44*(2), 238-246.

[42] Bilgin, N., Copur, H., & Balci, C. (2012). Effect of replacing disc cutters with chisel tools on performance of a TBM in difficult ground conditions. *Tunnelling and underground space technology*, *27*(1), 41-51.

[43] Chang, S. H., Choi, S. W., Bae, G. J., & Jeon, S. (2006). Performance prediction of TBM disc cutting on granitic rock by the linear cutting test. *Tunnelling and Underground Space Technology*, *21*(3), 271.

[44] Pan, Y., Liu, Q., Liu, J., Liu, Q., & Kong, X. (2018). Full-scale linear cutting tests in Chongqing Sandstone to study the influence of confining stress on rock cutting efficiency by TBM disc cutter. *Tunnelling and Underground Space Technology*, *80*, 197-210.

[45] Slob, E., Sato, M., & Olhoeft, G. (2010). Surface and borehole ground-penetrating-radar developments. *Geophysics*, *75*(5), 75A103-75A120.

[46] Daniels, D. J. (Ed.). (2004). *Ground penetrating radar* (Vol. 1). Iet.

[47] Okonkwo, V., Briggs, T., Paranjape, R., & van den Berghe, M. (2019, September). Numerical Modelling of Ground Penetrating Radar for Potash Mine Safety. In *10th International Workshop on Advanced Ground Penetrating Radar* (Vol. 2019, No. 1, pp. 1-7). European Association of Geoscientists & Engineers.

[48] Peters, L. P., Daniels, J. J., & Young, J. D. (1994). Ground penetrating radar as a subsurface environmental sensing tool. *Proceedings of the IEEE*, *82*(12), 1802-1822.

[49] Do, J. (2003). Report: Ground Penetrating Radar. *Villanova University: Pennsylvania*, 5.

[50] Haridim, M., & Zemach, R. (2021). Stochastic processes approach in GPR applications. *IEEE Transactions on Geoscience and Remote Sensing*, *60*, 1-10.

[51] Conyers, L. B. (2006). Ground-penetrating radar. *Remote sensing in archaeology: an explicitly north American perspective*, 131-160.

[52] Jol, H. M. (Ed.). (2008). *Ground penetrating radar theory and applications*. Elsevier.

[53] Balanis, C. A. (2024). *Balanis' Advanced Engineering Electromagnetics*. John Wiley & Sons.

[54] Aziz, A., Setyawati, O., Rahmadwati, R., & Bangert, A. (2018, October). Model simulation of ground penetrating radar using GPRMax to detect Porang tuber. In *2018 Electrical Power, Electronics, Communications, Controls and Informatics Seminar (EECCIS)* (pp. 136-141). IEEE.

[55] Savita, S. J., & Pallavi, A. (2022, April). Modeling of GPR Using gprMax Simulation. In *2022 IEEE International Conference on Distributed Computing and Electrical Circuits and Electronics (ICDCECE)* (pp. 1-4). IEEE.

[56] Giannopoulos, A. (2005). Modelling ground penetrating radar by GprMax. *Construction and building materials*, *19*(10), 755-762.

[57] Devereux, S. (1998). Practical well planning and drilling. *Pennwell, Oklahoma, Ok*.

[58] Allen, J. H. (1968). Drilling Large diameter holes. *Australian Oil and Gas Review*, 10 pp.

[59] Lyons, W. C. (2009). *Air and gas drilling manual: applications for oil and gas recovery wells and geothermal fluids recovery wells*. Elsevier.

[60] Tabor, D. (1954). Mohs's hardness scale-a physical interpretation. *Proceedings of the Physical Society. Section B*, *67*(3), 249.

[61] Amado, L. (2013). *Reservoir exploration and appraisal*. Gulf Professional Publishing.

[62] Han, X., Song, S., & Li, J. (2020). Pressure drop characteristics of reverse circulation pneumatic cuttings removal during coal seam drilling. *Science Progress*, *103*(2), 0036850420925235.

[63] Maurer, W. C. (1962). The" perfect-cleaning" theory of rotary drilling. *Journal of Petroleum Technology*, *14*(11), 1270-1274.

[64] Arvani, F., Sarker, M. M., Rideout, D. G., & Butt, S. D. (2014, September). Design and development of an engineering drilling simulator and application for offshore drilling for MODUs and deepwater environments. In *SPE Deepwater Drilling and Completions Conference*. OnePetro.

[65] Twidale, C. R. (2012). *Granite landforms*. Elsevier.

[66] Quan, W. (2021). *Experimental optimization of drilling, rock strength and backfilling for mining by drilling applications* (Doctoral dissertation, Memorial University of Newfoundland).

[67] Cigla, M., & Ozdemir, L. (2000, February). Computer modeling for improved production of mechanical excavators. In *SME Annual Meeting. Salt Lake City UT, USA*.

[68] Cigla, M., Yagiz, S., & Ozdemir, L. (2001, June). Application of tunnel boring machines in underground mine development. In *17th international mining congress and exhibition of Turkey* (pp. 155-164).

[69] Asbury, B., Ozdemir, L., & Rozgonyi, T. G. (2001). Frustum bit technology for continuous miner and roadheader applications. In *6th international symposium on mine mechanization and automation. S. Afr. Inst. Min. Met* (pp. 135-139).

[70] Asbury, B., Dezeeuw, M., Cigla, M., Ozdemir, L., & Oak Creek, C. (2003, February). Results of practical design modifications for respirable dust reduction on continuous miners in underground coal mining. In *Proceedings of the annual meeting of the society for mining, metallurgy and exploration (SME). Cincinnati, OH, Anonymous* (p. 9).

[71] Bilgin, N., Balci, C., Acaroglu, O., Tunçdemir, H., Eskikaya, S., Akgul, M., & Algan, M. (1999, May). The performance prediction of a TBM in Tuzla–Dragos sewerage tunnel. In *World Tunnel Congress* (pp. 817-822).

[72] Liu, B., Yang, H., & Karekal, S. (2020). Effect of water content on argillization of mudstone during the tunnelling process. *Rock Mechanics and Rock Engineering*, *53*, 799-813.

[73] Cao, L., Zhang, D., Fang, Q., & Yu, L. (2020). Movements of ground and existing structures induced by slurry pressure-balance tunnel boring machine (SPB TBM) tunnelling in clay. *Tunnelling and Underground Space Technology*, *97*, 103278.

[74] Frenzel, C., Käsling, H., & Thuro, K. (2008). Factors influencing disc cutter wear. *Geomechanik und Tunnelbau: Geomechanik und Tunnelbau*, *1*(1), 55-60.

[75] Zheng, YL, & He, L. (2021). TBM tunnel construction in extremely hard and extremely abrasive rocks: Problems, solutions and auxiliary rock breaking methods. *Journal of Central South University*, *28*, 454-480.

[76] RevoPoint POP 2 3D Scanner User Manual, 'https://www.revopoint3d.com/wpcontent/uploads/download/POP%202-Quick%20Start%20Guide.pdf'

[77] Li, Z. (2023). *Rock mass characterization using ground penetrating radar (GPR), rotary-percussion drilling performance, and indentation test* (Doctoral dissertation, Memorial University of Newfoundland).

[78] Aftab, A. A. R. I., Ismail, A. R., & Ibupoto, Z. H. (2017). Enhancing the rheological properties and shale inhibition behavior of water-based mud using nanosilica, multi-walled carbon nanotube, and graphene nanoplatelet. *Egyptian journal of petroleum*, *26*(2), 291-299.

[79] Bourgoyne, A.T., Millheim, K.K., Chenevert, M.E and Young F.S (1991). Applied drilling engineering. *SPE, Richardson, Texas*. Volume 2, pp 1-82.

[80] Anawe, P., & Folayan, A. (2018). *Advances in drilling fluids rheology*. LAP LAMBERT Academic Publishing.

[81] Radar, G. P. (2009). Ground penetrating radar: theory and applications. *Jol ISBN*, 978-0.

[82] Duan, Q., Duyn, J. H., Gudino, N., De Zwart, J. A., Van Gelderen, P., Sodickson, D. K., & Brown, R. (2014). Characterization of a dielectric phantom for high-field magnetic resonance imaging applications. *Medical physics*, *41*(10), 102303.--

[83] Merkle, H., Murphy-Boesch, J., Gelderen, P. V., Wang, S., Li, T. Q., Koretsky, A. P., & Duyn, J. H. (2011). Transmit B1-field correction at 7T using actively tuned coupled inner elements. *Magnetic Resonance in Medicine*, *66*(3), 901-910.

[84] Guo, X., Deng, H., & Fu, Q. (2020). An unusual decrease in dielectric constant due to the addition of nickel hydroxide into silicone rubber. *Composites Part B: Engineering*, *193*, 108006.

[85] Kato, H., & Ishida, T. (1987). Development of an agar phantom adaptable for simulation of various tissues in the range 5-40 mhz. (hyperthermia treatment of cancer). *Physics in Medicine & Biology*, *32*(2), 221.

[86] Okano, Y., Ito, K., Ida, I., & Takahashi, M. (2000). The SAR evaluation method by a combination of thermographic experiments and biological tissue-equivalent phantoms. *IEEE Transactions on Microwave Theory and Techniques*, *48*(11), 2094-2103.

[87] Ito, K., Furuya, K., Okano, Y., & Hamada, L. (2001). Development and characteristics of a biological tissue-equivalent phantom for microwaves. *Electronics and Communications in Japan (Part I: Communications)*, *84*(4), 67-77.

[88] Graedel, N. N., Polimeni, J. R., Guerin, B., Gagoski, B., & Wald, L. L. (2015). An anatomically realistic temperature phantom for radiofrequency heating measurements. *Magnetic resonance in medicine*, *73*(1), 442-450.

[89] Chou, C. K., Chen, G. W., Guy, A. W., & Luk, K. H. (1984). Formulas for preparing phantom muscle tissue at various radiofrequencies. *Bioelectromagnetics: Journal of the Bioelectromagnetics Society, The Society for Physical Regulation in Biology and Medicine, The European Bioelectromagnetics Association*, *5*(4), 435-441.

[90] Fukunaga, K., Watanabe, S., Asou, H., & Sato, K. (2005, June). Dielectric properties of non-toxic tissue-equivalent liquids for radiowave safety tests. In *IEEE International Conference on Dielectric Liquids, 2005. ICDL 2005.* (pp. 425-428). IEEE.

[91] Lopresto, V., Pinto, R., Lodato, R., Lovisolo, G. A., & Cavagnaro, M. (2012). Design and realisation of tissue-equivalent dielectric simulators for dosimetric studies on microwave antennas for interstitial ablation. *Physica Medica*, *28*(3), 245-253.

[92] Stauffer, P. R., Rossetto, F., Prakash, M., Neuman, D. G., & Lee, T. (2003). Phantom and animal tissues for modelling the electrical properties of human liver. *International journal of hyperthermia*, *19*(1), 89-101.

[93] Hartsgrove, G., Kraszewski, A., & Surowiec, A. (1987). Simulated biological materials for electromagnetic radiation absorption studies. *Bioelectromagnetics: Journal of the Bioelectromagnetics Society, The Society for Physical Regulation in Biology and Medicine, The European Bioelectromagnetics Association*, *8*(1), 29-36.

[94] Kanda, M. Y., Ballen, M., Salins, S., Chou, C. K., & Balzano, Q. (2004). Formulation and characterization of tissue equivalent liquids used for RF densitometry and dosimetry measurements. *IEEE Transactions on microwave theory and techniques*, *52*(8), 2046-2056.

[95] Akgun, C., DelaBarre, L., Snyder, C. J., Adriany, G., Gopinath, A., Ugurbil, K., & Vaughan, J. T. (2010). RF field profiling through element design for high field volume coils. In *ISMRM ESMRMRB Joint Annual Meeting (International Society for Magnetic Resonance in Medicine, Stockholm Sweden, 2010)* (p. 243& M).

[96] Eskandani, M., Hamishehkar, H., & Ezzati Nazhad Dolatabadi, J. (2013). Cyto/Genotoxicity study of polyoxyethylene (20) sorbitan monolaurate (tween 20). *DNA and cell biology*, *32*(9), 498-503.

[97] Das, S., Mondal, S., & Ghosh, S. (2013). Physicochemical studies on the micellization of cationic, anionic, and nonionic surfactants in water–polar organic solvent mixtures. *Journal of Chemical & Engineering Data*, *58*(9), 2586-2595.

[98] Autio, J., & Kirkkomäki, T. (1996). *Boring of full scale deposition holes using a novel dry blind boring method* (No. SKB-TR--96-21). Swedish Nuclear Fuel and Waste Management Co..

[99] Mitchell, R. F., & Miska, S. (2011). Fundamentals of drilling engineering. *(No Title)*.

Appendix

Appendix 1: Standard of Procedure for Scanning Rock Specimen

- On the main menu panel, click on the scan Tab.

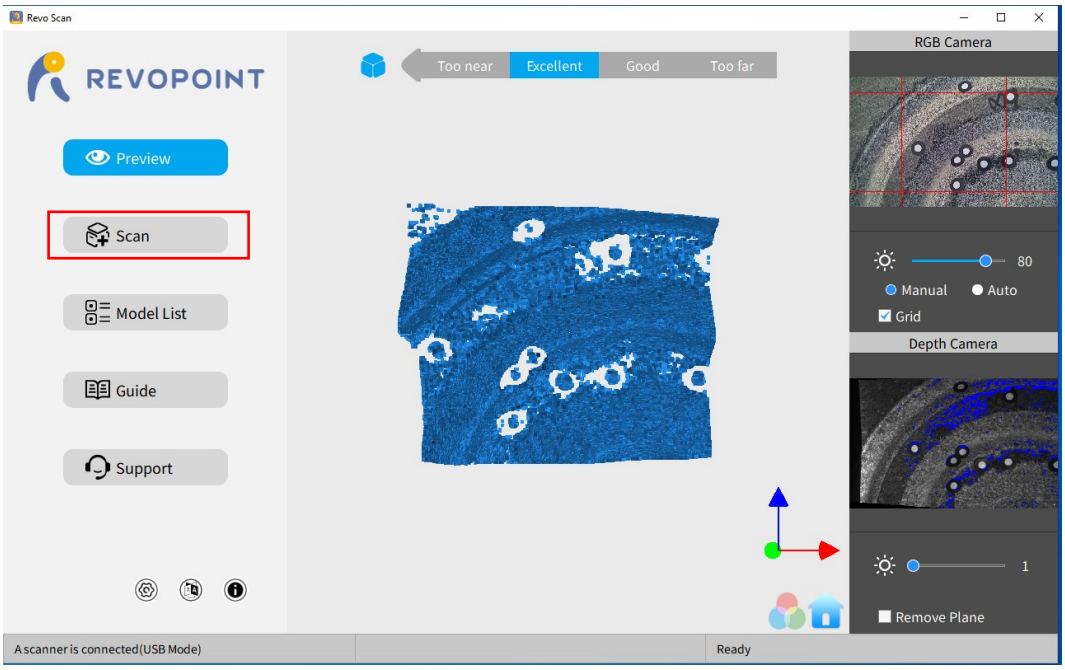

- Followed by new scan and the scan setting is adjusted based on the work to be done. In our case a drilled groove profile is to be scanned. Document name is set, Accuracy is selected as high accuracy scan, scan mode is selected as marker for drilled rock specimen as described earlier, and texture as no color as only the shape information is of importance.

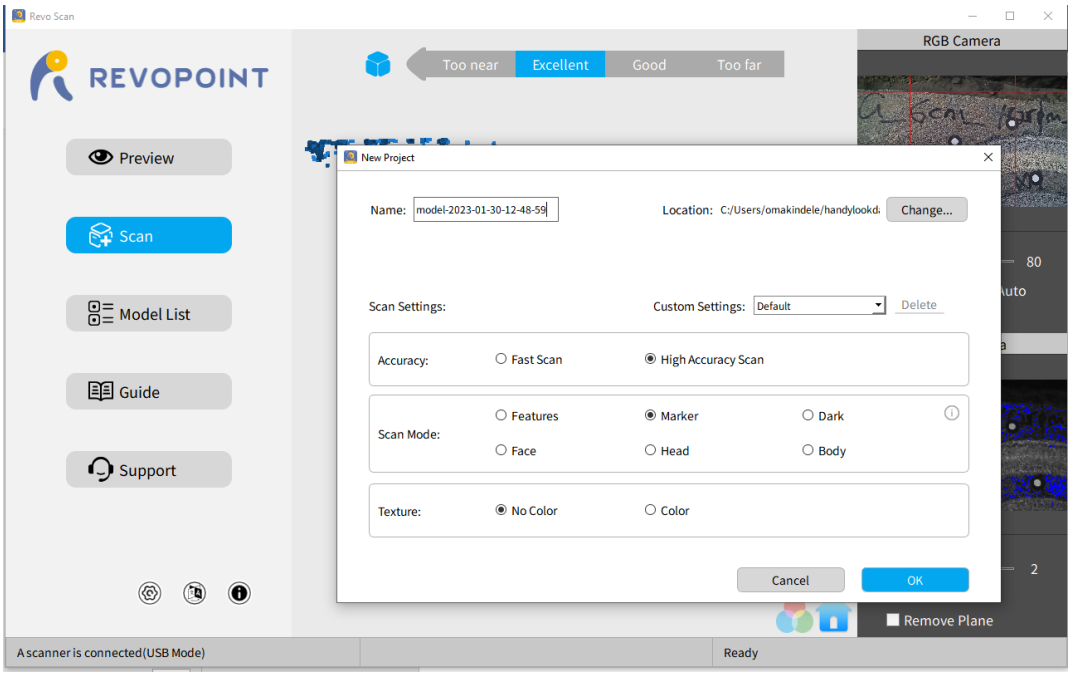

- Distance is confirmed and maintained to be excellent to ensure a quality scan with high resolution. Too far and too near won't scan the specimen. To start scanning, click on the play symbol tab.

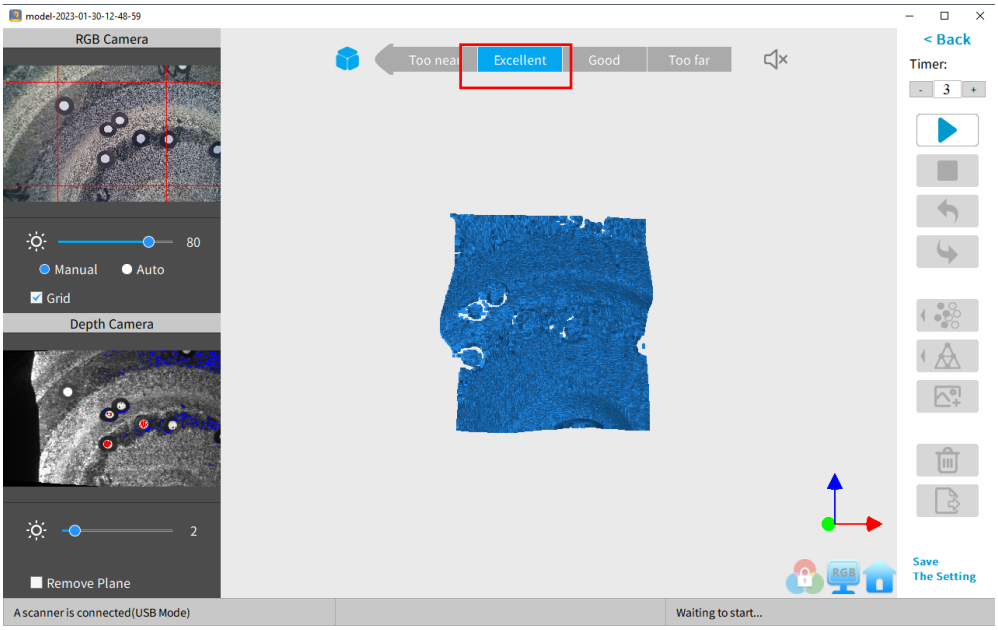

- During scanning, the scanner is moved gently and deliberately while maintaining a largely constant distance. Advisable to start from the center of the rock specimen.

- Once all the groove is captured, complete scan by clicking the stop symbol tab.

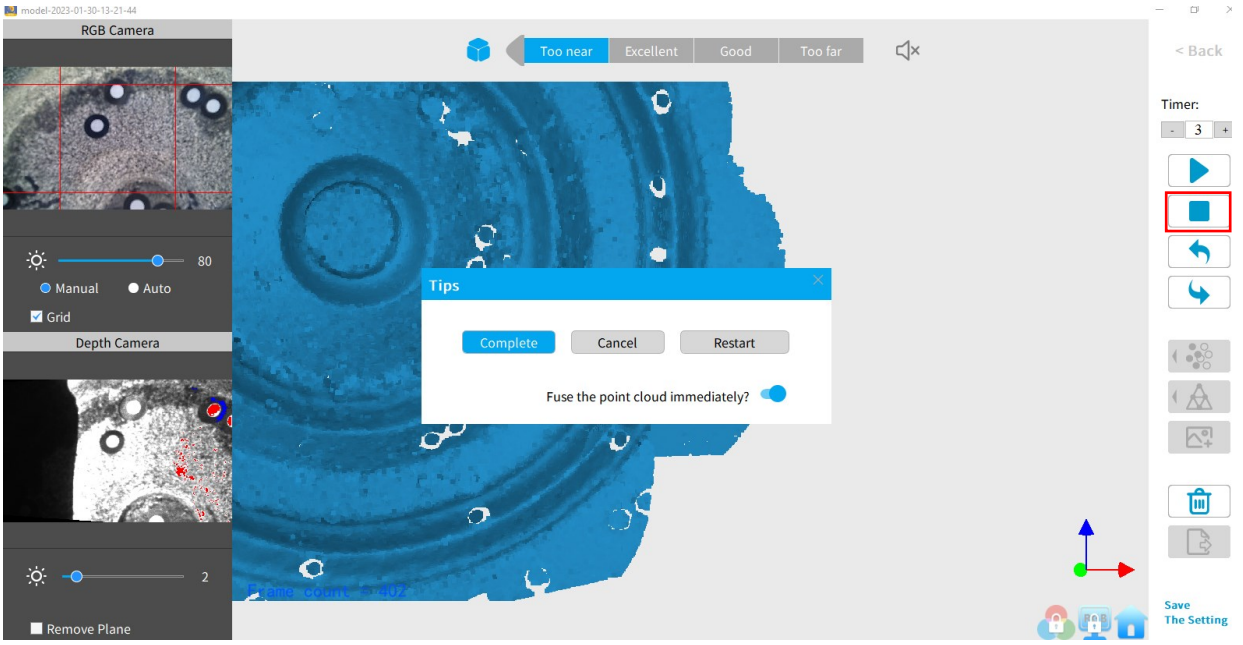

- Fuse the point cloud data

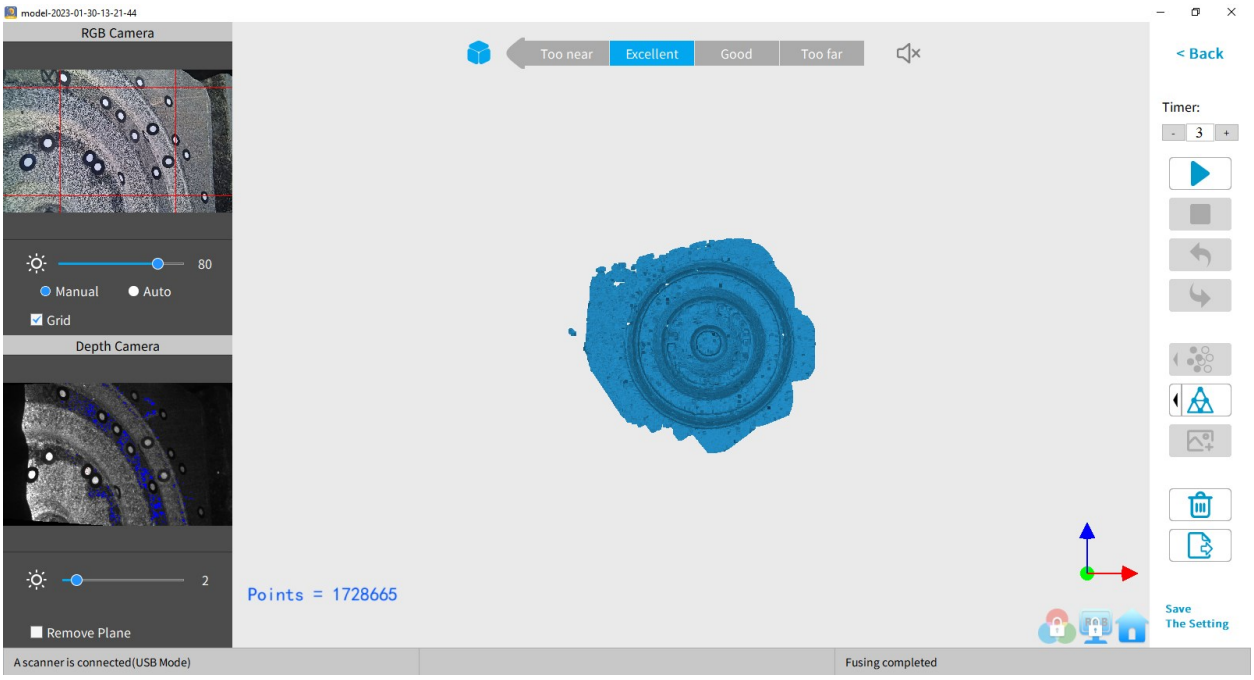

- Mesh to convert the scanned point cloud data

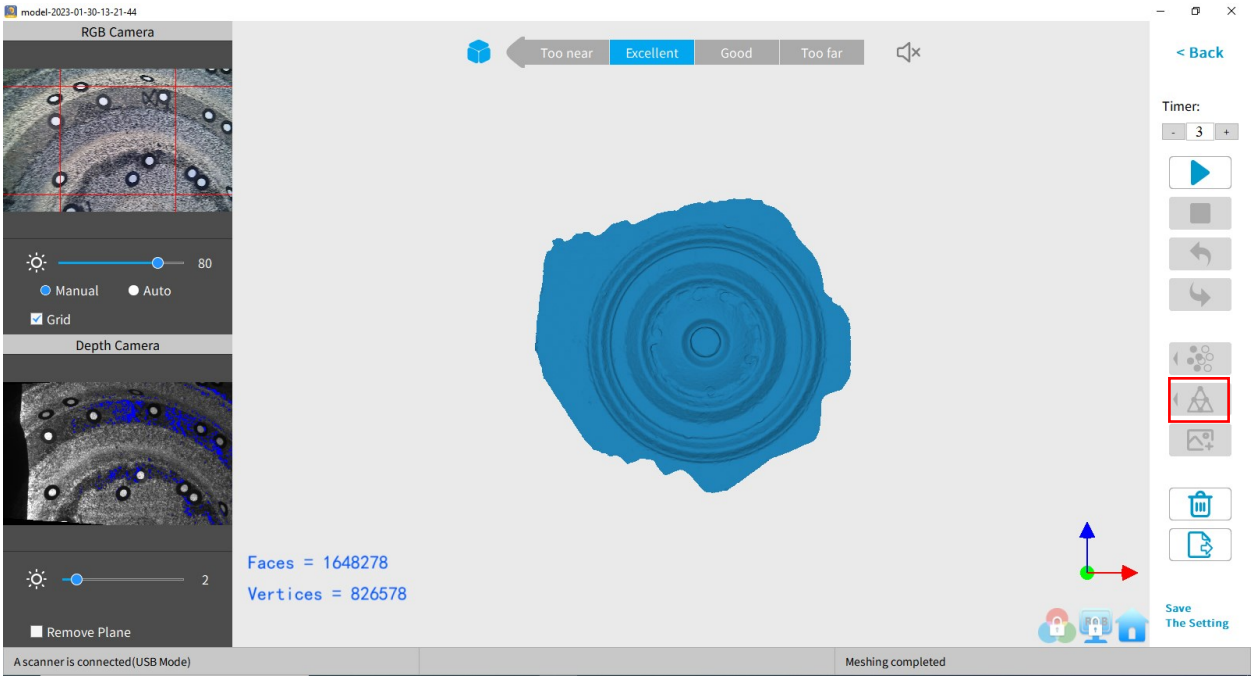

- Export the 3D model as a file format (.PLY, .OBJ or .STL are supported). Advisable to export into a STL file format as that seems to be highly supported on solidworks for analysis.

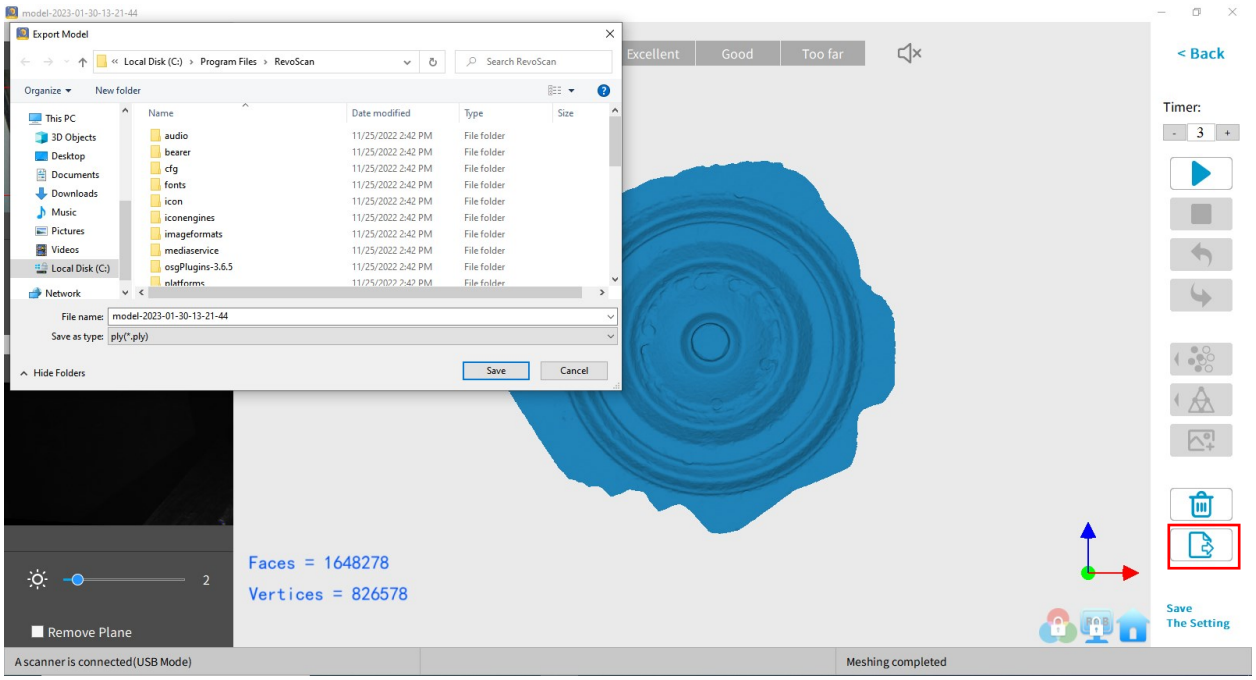

Appendix 2: Properties of Microbarite over API barite

MICROBAR is a high-quality, micronized barite (barium sulphate) used as weighting agent in water based and oil based drilling fluids.

Typical Physical Properties

Physical appearance.....Grey to white, reddish powder
Bulk density. .....1920 - 2160 kg/m³ (120 -135 lb/ft³)
Specific gravity.....4.20 minimum
Temperature stability.....Normally stable
Solubility.....Insoluble in water and oil
Freezing / Melting / Pour point.... .....1350°C (2462°F)
pH.....Neutral
Particle Size Distribution .....d_{50}=2 – 6 µm, d_{90}=10 – 24 µm

Applications

MICROBAR is used to increase the density of any drilling fluid systems. The micronized particle size enables low rheology fluids to be formulated with considerably reduced risk of barite sag and settlement compared to fluids formulated with API drilling grade barite. In addition, the low rheology of the fluid will result in lower ECD's, giving the option of either higher flow rates or lower pump pressures.

MICROBAR is used as the weighting agent for the non-aqueous fluid EMS-4750.

The amount of MICROBAR required to increase the density of the drilling fluid can be calculated with the following formulas:

$$\text{MICROBAR, kg/m}^3 = 4200 \times \frac{(W_2 - W_1)}{(4{,}20 - W_2)}$$

Where:
W_1 = Initial mud weight as specific gravity
W_2 = Desired mud weight as specific gravity